Arabian Journal of Chemistry (2022) **15**, 103595

King Saud University

Arabian Journal of Chemistry

www.ksu.edu.sa
www.sciencedirect.com

ORIGINAL ARTICLE

A possible potential COVID-19 drug candidate: Diethyl 2-(2-(2-(3-methyl-2-oxoquinoxalin-1(2H)-yl)acetyl)hydrazono)malonate: Docking of disordered independent molecules of a novel crystal structure, HSA/DFT/XRD and cytotoxicity

Mohcine Missioui [a], Musa A. Said [b], Güneş Demirtaş [c], Joel T. Mague [d], Ahlam Al-Sulami [e], Nadia S. Al-Kaff [b], Youssef Ramli [a,*]

[a] *Laboratory of Medicinal Chemistry, Drug Sciences Research Center, Faculty of Medicine and Pharmacy, Mohammed V University in Rabat, Morocco*
[b] *College of Science, Taibah University, PO Box 30002, Al-Madinah Al Munawarah, 1417, Saudi Arabia*
[c] *Ondokuz Mayıs University, Faculty of Arts and Sciences, Department of Physics, 55139 Samsun, Turkey*
[d] *Department of Chemistry, Tulane University, New Orleans, LA 70118, USA*
[e] *Department of Chemistry, College of Science, University of Jeddah, Jeddah 21589, Saudi Arabia*

Received 21 September 2021; accepted 24 November 2021
Available online 28 November 2021

KEYWORDS

Malonate-based quinoxaline;
Crystal structure;
COVID-19;
DFT;
In silico molecular docking;
Hirshfeld surface analysis (HSA);
ADMET;
PASS

Abstract This study reports the synthesis, characterization and importance of a novel diethyl 2-(2-(2-(3-methyl-2-oxoquinoxalin-1(2H)-yl)acetyl)hydrazono)malonate (**MQOAHM**). Two independent molecular structures of the disordered **MQOAHM** have been established by XRD single crystal analysis in a ratio of 0.596(3)/0.404(3), **MQOAHM (a)** and **MQOAHM (b),** respectively. **MQOAHM** was characterized by means of various spectroscopic tools ESI-MS, IR, ^{1}H &^{13}C NMR analyses. Density Functional Theory (DFT) method, B3LYP, 6–311 + + G(d,p) basis set was used to optimize **MQOAHM** molecule. The obtained theoretical structure and experimental structure were superimposed on each other, and the correlation between them was calculated. The Highest Occupied Molecular Orbital (HOMO) and Lowest Unoccupied Molecular Orbital (LUMO) were created, and the energy gap between these orbitals was calculated. For analyzing intermolecular interactions, Molecular Electrostatic Potential (MEP) and Hirshfeld Surface Analysis were studied. For a fair comparative study, the two forms of the title compound were

* Corresponding author.
E-mail address: y.ramli@um5s.net.ma (Y. Ramli).
Peer review under responsibility of King Saud University.

Production and hosting by Elsevier

https://doi.org/10.1016/j.arabjc.2021.103595

docked together with 18 approved drugs and **N3** under precisely the same conditions. The disordered molecule structure's binding scores against 7BQY were −7.0 and −6.9 kcal/mol^{-1} for **MQOAHM (a)** and **MQOAHM (b)**, respectively. Both the forms show almost identical superimposed structures and scores indicating that the disorder of the molecule, in this study, has no obvious effect. The high binding score of the molecule was attributed to the multi-hydrogen bond and hydrophobic interactions between the ligand and the receptor's active amino acid residues. Worth pointing out here that the aim of using the free energy *in Silico* molecular docking approach is to rank the title molecule compared to the wide range of approved drugs and a well-established ligand **N3**. The binding scores of all the molecules used in this study are ranged from −9.9 to −4.5 kcal/mol^{-1}. These results and the supporting statistical analyses suggest that this malonate-based ligand merits further research in the context of possible therapeutic agents for COVID-19. Cheap computational techniques, PASS, Way2drug and ADMET, online software tools, were used in this study to uncover the title compound's potential biological activities and cytotoxicity.

1. Introduction

Severe acute respiratory syndrome coronavirus 2 (SARS-CoV-2), the causative agent of Coronavirus Disease 2019 (COVID-19), is a novel beta-coronavirus first identified in December 2019 in Wuhan, China. As of 20 September 2021, there have been 219.113.953 confirmed cases of this disease, including 4.570.041 deaths in 216 countries, reported to the World Health Organization (WHO). The US Food and Drug Administration (FDA) approved only remdesivir for the treatment of COVID-19 (Parsey, 2020). However, several reports proposed agents to treat COVID-19 include direct antivirals (Cao et al., 2020), baricitinib (Cantini et al., 2020), hydroxychloroquine (Sogut et al., 2021), glucocorticoids (Russell et al., 2020) and anakinra (Pasin et al., 2021; Cavalli et al., 2020). Researchers have made great progress in the development of potential medical treatments in response to the COVID-19 pandemic. Currently, several molecules are being tested for their efficiency on COVID-19 disease, some of which have reached clinical trials, while others are still in the preclinical phase (Sanders et al., 2020; Luo et al., 2020; Colaneri et al., 2020; Quartuccio et al., 2020; Campochiaro et al., 2020). Quinoxaline as a wonder nucleus in the fused systems of nitrogen-containing heterocycles, is important nitrogenous hetero compound due to their extensive properties, (Ramli and Essassi, 2015; Ramli et al., 2014; Zarrok et al., 2012; Tazouti et al., 2016; El Aoufir et al., 2016; Laabaissi et al., 2019) and shows a variety of activities in the medical field, including analgesic (Dewangan et al., 2018), anti-inflammatory (Shen et al., 2020)anti-tubercular (Srinivasarao et al., 2020), anti-bacterial (Patel et al., 2019), bacteriocides (Thakuria and Das, 2006), anti-HIV (Patel et al., 2016), anti-diabetic (Kulkarni et al., 2012), anti-oxydant (Missioui et al., 2021) and anti-cancer (Guerreiro et al., 2020; Abad et al., 2021) agents. Malonate-based compounds have aroused increasing attention because of their important pharmacological activities, such as decreased blood glucose (Shinkai et al., 1998) anti-HIV (Serafin et al., 2011) anticancer (Xing et al., 2012) anti-inflammatory (Kim et al., 2001) antioxidative (Saranya et al., 2013) and antiviral (Xiao et al., 2014) activities. Moreover, malonates are traditionally regarded as important materials for synthesizing the key intermediates of numerous active substances (Wheeler, 1984; Woo et al., 1989; Ragoussis et al., 2004; Brandau et al., 2006). The binding affinity and structure of protein-drug complexes play an important role in understanding the molecular mechanism in drug discovery. Moreover, the SARS-CoV-2 main protease is a key target for COVID-19 drug discovery. Based on the above findings and our interest in developing novel and promising pharmacological agents (Zaoui et al., 2021; Abad et al., 2021; Abad et al., 2021; Guerrab et al., 2021; Guerrab et al., 2020; Guerrab et al., 2021), including anti COVID-19 drug (Abdel-Rahman et al., 2022; Missioui et al., 2022); a malonate-based derivative containing oxoquinoxalin-1(2H)-yl)acetohydrazide moiety MQOAHM was synthesized and characterized. In addition, the molecular structure was confirmed by single-crystal X-ray diffraction studies. The theoretical molecular geometry of this compound was found by DFT calculation, and the obtained structure was compared with the experimental structure. FOMs and MEP graphics were plotted, and the energy gap between HOMO and LUMO was calculated. For analyzing the intermolecular hydrogen bonds, Hirshfeld surface analysis was studied.

Additionally, for a comparative study and ranking the title compound to the approved drugs, the title compound was docked together with 18 approved drugs and N3 under the same conditions. This study aimed to rank the title compound, MQOAHM with respect to a wide range of approved drugs and the well-established inhibitor, **N3.** Moreover, the biological and cytotoxicity activities prediction of this novel compound was carried out. Finally, in silico ADMET screening was also performed.

2. Experimental section

2.1. Synthesis

All commercial chemicals were purchased from Sigma-Aldrich and used as received. TLC follow-up of the reaction to check the compound's purity was made out on silica gel-precoated aluminium sheets (Fluorescent indicator 254 nm, Fluka, Germany). The spots were detected by exposure to UV lamp at λ 254/366 nm for a few seconds. The melting point was obtained on a Büchi Melting Point SMP-20 apparatus and is uncorrected. The ^{1}H NMR and ^{13}C NMR spectra were recorded on a Bruker Avance 300 NMR Spectrometer in DMSO d_6. The chemical shifts δ were reported in parts per

million (ppm); the IR spectrum was obtained using the Bruker-VERTEX 70 device and the associated software OPUS, an ATR (attenuated total reflectance) mode. Mass spectra were recorded on an API 3200 LC/MS/MS mass spectrometer using electrospray ionization (ESI) in positive polarity.

2.1.1. 3-Methyl-1H-quinoxalin-2-one (MQO)

Following a procedure similar to that of Hinsberg (Ramli and Essassi, 2015), we have successfully synthesized 3-methyl-1H-quinoxalin-2-one with a yield of 91% by condensation of *O*-phenylenediamine (10 mmol) with ethyl pyruvate (15 mmol) in HCl 4 N aqueous solution for 30 min at room temperature, Scheme 1.

2.1.2. Ethyl 2-(3-methyl-2-oxo-1,2-dihydroquinixalin-1-yl) acetate (EMQOA)

To a solution of 3-methylquinoxalin-2(1*H*)-one (3 g, 18.7 mmol) in *N,N*-dimethylformamide (15 mL) were added ethyl 2-bromoacetate (4.7 mL, 28.5 mmol), potassium carbonate (3.6 g, 28.5 mmol) and a catalytic quantity of tetra-nbutylammonium bromide. The reaction mixture was stirred at room temperature for 24 h. The solution was filtered, and the solvent was removed under reduced pressure. The solid obtained was recrystallized from ethanol solution to afford a white powder, ethyl 2- (3-methyl-2-oxoquinoxalin-1 (2H)-yl) acetate (EMQOA), with a yield of 72%.

2.1.3. 2-(3-methyl-2-oxoquinoxalin-1(2H)-yl)acetohydrazide (MQOAH)

To the formed residue (EMQOA) (1 g, 4 mmol) taken in ethanol (20 mL) was added hydrazine hydrate (0.3 mL, 6 mmol), then left stir for 24 h at room temperature. The target compound, 2-(3-methyl-2-oxoquinoxalin-1(2H)-yl)acetohydrazide (MQOAH) precipitate and recrystallized from ethanol, the yield is around 77%, Scheme 1.

2.1.4. 2-(2-(2-(3-methyl-2-oxoquinoxalin-1(2H)-yl)acetyl) hydrazono)malonate (MQOAHM)

In ethanol (15 mL), to this quinoxaline(0.5 g, 2.1 mmol) was added (0.7 mL, 4.2 mmol) of diethyl 2-oxomalonate, stirred for 2 h under reflux at 80 °C. The mixture then was filtered and the solvent evaporated under reduced pressure, and the residue was crystallized from its ethanol solution. The reaction yield is 65%. Scheme 1. The compound was dissolved in ethanol and left for slow evaporation to afford a colourless plate-like crystal, Fig. 1.

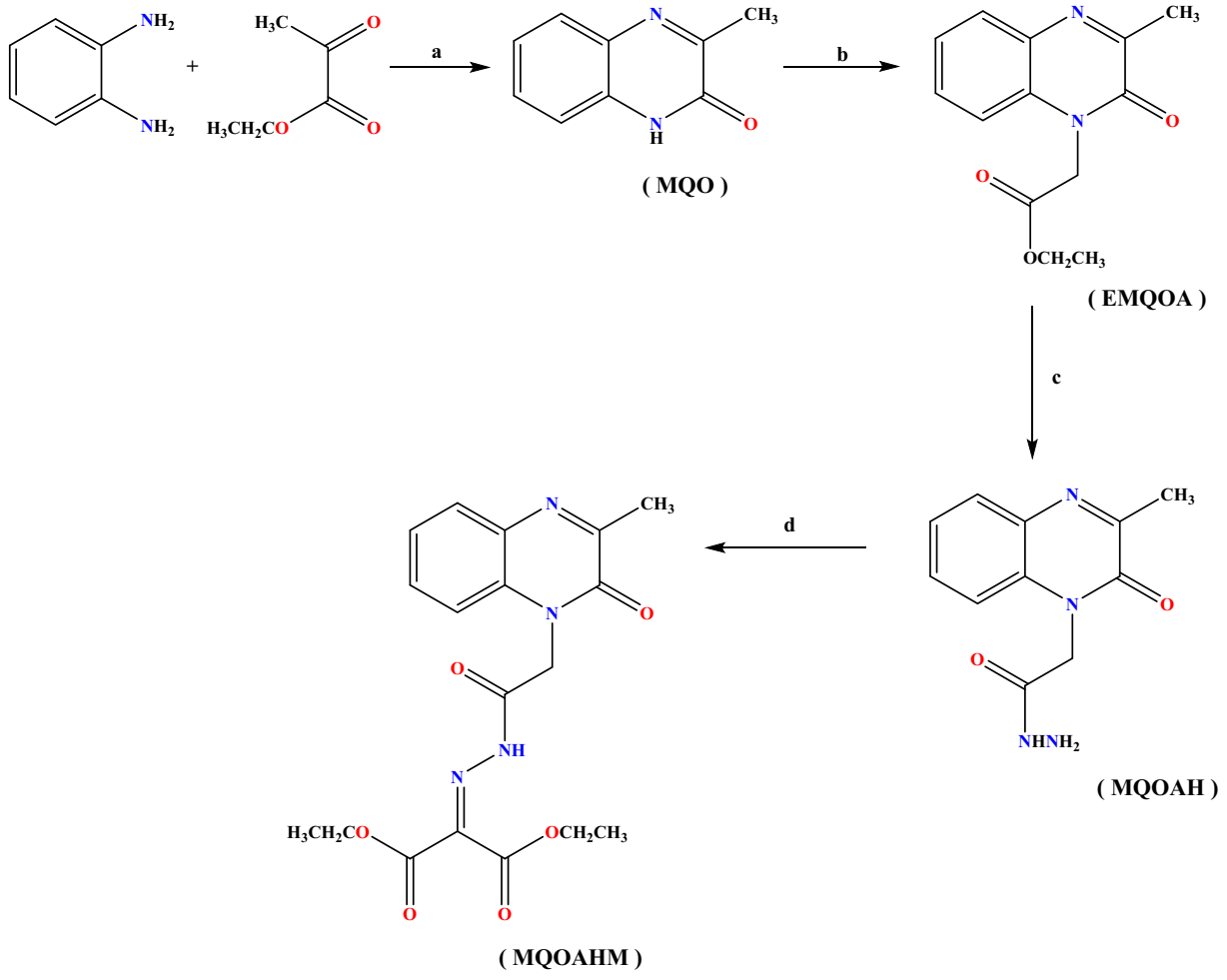

Scheme 1 Synthesis procedure for the preparation of (MQOAHM); Reagents: a) HCl 4 N; b) Bromoethylacetate, K_2CO_3, BTBA, DMF; c) $NH_2NH_2{\cdot}H_2O$, EtOH; d) diethyl-2-oxomalonate, EtOH.

Fig. 1 An image of MQOAHM crystals.

2.2. Crystal structure determination

A colourless plate-like specimen of $C_{18}H_{20}N_4O_6$, approximate dimensions 0.032 mm × 0.230 mm × 0.303 mm, was used for the X-ray crystallographic analysis. The X-ray intensity data were measured on a Bruker Smart APEX CCD system equipped with a fine-focus sealed tube (Mo-Kα, λ = 0.7 1073 Å) and a graphite monochromator. The complete sphere of data was processed using SAINT (Bruker, 2016). The structure (Fig. 2) was solved by direct methods and refined by the full-matrix least-squares method on F2 using SHELXT and SHELXL programs (Sheldrick, 2015a; Sheldrick, 2015b). The molecular and packing diagrams were generated using DIAMOND (Brandenburg and Putz, 2012). Crystal and refinement details are presented in Table 1.

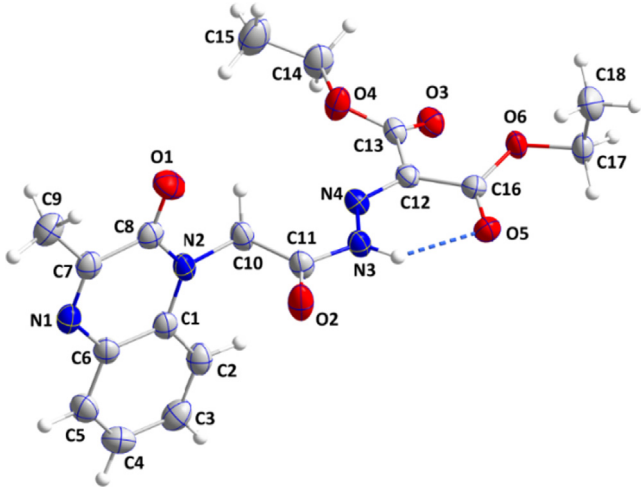

Fig. 2 ORTEP view of the title compound indicating the atom-numbering scheme. Displacement ellipsoids are illustrated at the 50% probability level.

Table 1 Crystal data and structure refinement details for MQOAHM.

Value	Parameter
Chemical formula	$C_{18}H_{20}N_4O_6$
M_r	388.38
Crystal system, space group	Monoclinic, $P2_1/c$
Temperature (K)	150
a, b, c (Å)	4.7504 (3), 22.2791 (16), 17.3723 (12)
B (°)	90.076 (1)
V (Å^3)	1838.6 (2)
Z	4
Radiation type	Mo $K\alpha$
μ (mm^{-1})	0.11
Crystal size (mm)	0.30 × 0.23 × 0.03
Diffractometer	Bruker Smart *APEX* CCD
Absorption correction	Multi-scan *SADABS* (Krause et al., 2015).
T_{min}, T_{max}	0.87, 1.00
No. of measured, independent and observed [$I > 2\sigma(I)$] reflections	17274, 4563, 3100
R_{int}	0.035
(sin θ/λ)$_{max}$ (Å^{-1})	0.669
$R[F^2 > 2\sigma(F^2)]$, $wR(F^2)$, S	0.051, 0.142, 1.05
No. of reflections	4563
No. of parameters	265
H-atom treatment	H-atom parameters constrained
$\Delta\rho_{max}$, $\Delta\rho_{min}$ (e Å^{-3})	0.28, −0.17

CCDC 2062620 contains the supplementary crystallographic data for this paper. These data can be obtained free of charge via http://www.ccdc.cam.ac.uk/conts/retrieving.html (or from the Cambridge Crystallographic Data Centre, 12, Union Road, Cambridge CB2 1EZ, UK; fax: +44 1223 336033).

2.3. Computational procedure

2.3.1. Hirshfeld surface analysis (HAS)

HAS and the related 2D-fingerprint plots were calculated for diethyl-2-(2-(2-(3-methyl-2-oxoquinoxalin-1(2H)-yl)acetyl)hydrazono)malonate MQOAHM **(a)**, using Crystal Explorer, Version 17, which reads CIF format as an X-ray input file (Turner et al., 2017). The cut-off for the hydrophobic interactions between the amino acid residues and the ligands is 3.9 Å (Tanoli et al., 2020).

2.3.2. Density Functional Theory (DFT)

Geometric optimization of the molecule was executed with Gaussian 09 W package program (Frisch et al., 2010) and was calculated by using Density Functional Theory (DFT) method by B3LYP (Becke's three-parameter hybrid functional using the LYP correlation functional) with 6–311 + + G(d,p) basis set. For modeling, initial values were obtained X-ray diffraction. Molecular electrostatic potential map and molecular orbitals were plotted with Gauss-View 5 molecular visualization program (Dennington et al., 2009).

2.4. Docking in silico studies

Docking calculations of **MQOAHM (a)** and 20 approved drugs were accomplished using the Autodock Vina wizard in PyRx 0.8 (Trott and Olson, 2009). The occupancies of the disordered ligand crystal are 0.593(2) MQOAHM **(a)**/0.404(3) MQOAHM **(b)**. Settings are made the same in the program for all docked molecules in this study, which include: Grid box center_x = 6.99668717076, center_y = 0.922958951594, center_z = 22.8078934645, size_x = 19.4420049859, size_y = 26.6047156615 and size_z = 26.841321877. Our ligand's energy minimization, 20 approved drugs and protein, was performed using the default settings in the Autodock Vina-PyRx. The CIF files of the MQOAHM **(a,b)** (CCDC = 2062620). All drugs and ligands were converted to PDB file type using Mercury package (Macrae et al., 2006) and were used as input to Autodock vina in PyRx. The proteases (PDB code 7BQY) were saved in PDB format after deleting the water molecules and ligands using Discovery Studio Visualizer v17.2.0.16349. The PyMOL molecular viewer was used to present the output (DeLano, 2004). Schematic diagrams of protein–ligand interactions were generated using the LIGPLOT program (Wallace et al., 1995).

3. Results and discussion

3.1. Synthesis and crystallisation of diethyl 2-(2-(2-(3-methyl-2-oxoquinoxalin-1(2H)-yl)acetyl)hydrazono)malonate (MQOAHM)

3.1.1. 3-Methyl-1H-quinoxalin-2-one (MQO)

Yield 91%, mp = 219.3–220.5 °C, FT-IR (ATR, υ, cm^{-1}) 1568 υ (C═N), 1663 υ (C═O), 2710, 2843, 2898, 2963, 3007 υ(C—H, aromatic), 3430 υ (N—H). 1H NMR (DMSO d_6) δ ppm: 2.40 (3H, s, CH3), 7.27 (2H, m, Harom), 7.28 (1H, d, J = 8.86 Hz, H arom), 12.29 (1H, s, N—H). 13C NMR (DMSO d_6) δppm: 20.51 (CH3), 115.22, 123.04, 127.86, 129.31 (C-HArom), 131.65 (Carom-N), 131.91 (Carom-N), 159.22 (C═O); HRMS (ESI-MS) (m/z) calculated for $C_9H_8N_2O$ 160.06, found 160.17.

3.1.2. Ethyl 2-(3-methyl-2-oxo-1,2-dihydroquinixalin-1-yl) acetate (EMQOA)

Yield 72%, color: white, mp = 140.5–142.3 °C, FT-IR (ATR, υ, cm^{-1}) 1168 υ (N—C $_{amide}$), 1600 υ (C═C_{arom}), 1645 υ (C═O $_{amide}$), 3051 υ(C—H_{arom}), 2961 υ(C-H,CH_2), 1213 υ (C—O $_{ester}$), 1737 υ (C═O $_{ester}$), ^{1}H NMR (DMSO d_6) δ ppm: 2.48 (3H, s, CH_{3Qinx}); 1.24 (3H, t, J = 1.4 Hz,$CH_{3\text{-}ester}$), 5.11 (2H, s, CH_2), 4.19 (2H, q, J = 1.4 Hz, $CH_{2\text{-}ester}$), 7.39–7.82 (4H, m, J = 1.3 Hz, H_{arom}), ^{13}C NMR (DMSO d_6) δppm: 43.56 (CH_{2Qinx}), 61.33 (CH_2 $_{ester}$), 20.99 (CH_3 $_{Qinx}$), 13.98 (CH_3 $_{ester}$), 154.15 (C═N $_{Qinx}$), 157.47 (C═O $_{amide}$), 114.46–132.83 (C_{Ar}), 167.50 (C═O $_{ester}$); Its mass spectrum showed a molecular ion peak (MH+, m/z = 247.10739) which conforms to its molecular formula $C_{13}H_{14}N_2O_3$.

3.1.3. 2-(3-methyl-2-oxoquinoxalin-1(2H)-yl)acetohydrazide (MQOAH)

Yield 77%, color: white, mp = 183.5–182.3 °C, FT-IR (ATR, υ, cm^{-1}) 1168 υ (N-C $_{amide}$), 1600 υ (C═C_{arom}), 1645 υ (C═O $_{amide}$), 3051 υ(C—H_{arom}), 2961 υ(C—H,CH_2), ^{1}H NMR (DMSO d_6) δ ppm: 2.46 (3H, s, CH_{3Qinx}), 5.11 (2H, s, CH_2),

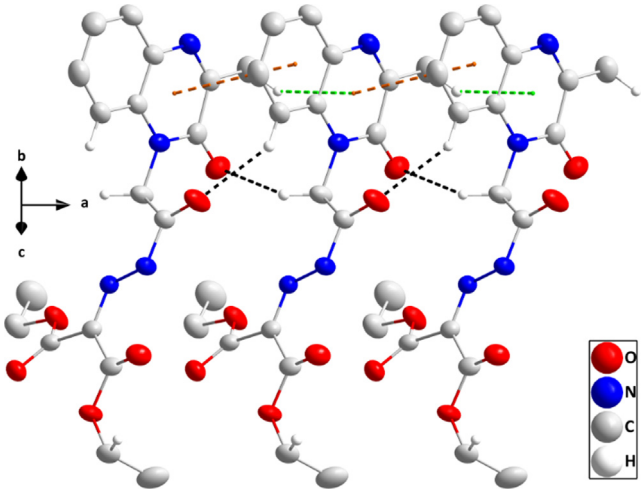

Fig. 3 A portion of one oblique stack projected onto (011). C—H···O hydrogen bonds are depicted by black dashed lines while π-stacking and C—H···π(ring) interactions are shown, respectively, by orange and green dashed lines.

Table 2 Hydrogen-bond geometry (Å, °).

Cg1 is the centroid of the C1/C6/N1/C7/C8/N2 ring.

D—H···*A*	*D*—H	H···*A*	*D*···*A*	*D*—H···*A*
N3—H3A···O5	0.91	2.02	2.6865(18)	128
C2—H2···O2^{i}	0.95	2.40	3.213(2)	144
C9—H9A···Cg1^{ii}	0.99	2.72	3.473(2)	134
C10—H10B···O1^{i}	0.99	2.58	3.290(2)	128
C17—H17B···O2^{iii}	0.99	2.35	3.154(5)	138

Symmetry codes: (i) $x-1, y, z$; (ii) $x+1, y, z$; (iii) $-x+2, -y+1, -z+1$.

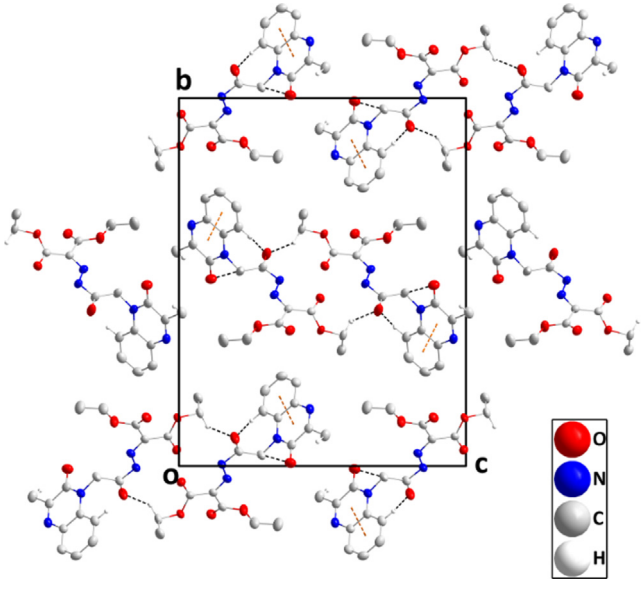

Fig. 4 Packing viewed along the a-axis direction with intermolecular interactions depicted as in Fig. 3.

4.17(s,2H,NH_2), 10.44 (s,1H,–NH-NH_2), 7.39–7.82 (4H, m, J = 1.3 Hz, H_{arom}), ^{13}C NMR (DMSO d_6) δppm: 43.56 (CH_{2Qinx}), 20.99 ($CH_{3\ Qinx}$), 154.15 (C═N $_{Qinx}$), 157.47 (C═O $_{amide}$), 114.46–132.83 (C_{Ar}); Its mass spectrum showed a molecular ion peak (MH+, m/z = 232.10318) which conforms to its molecular formula $C_{11}H_{12}N_4O_2$.

3.1.4. 2-(2-(2-(3-methyl-2-oxoquinoxalin-1(2H)-yl)acetyl) hydrazono)malonate (MQOAHM)

Yield 65%, color: Pale yellow, mp = 236.5 – 238.3 °C, FT-IR (ATR, υ, cm-1): 3215 υ(N─H $_{amide}$), 1698 υ(C═O $_{amide}$), 1604 υ(C═C_{arom}), 1409 υ(C─H $_{CH3qin}$), 2973 υ($CH_{3\ streching}$), 1733 υ (C═O $_{ester}$), 1655 υ(C═O_{amid}), 1162 υ(C─O $_{ester}$); ^{1}H NMR (DMSO d_6) δ ppm: 2.48 (s, 3H, $CH_{3,quin}$), 5.41 (s, 2H, CH_2), 12.26 (s, 1H, NH), 1.29 (t, 3H, J = 8,1 Hz), 4.34 (q, 2H, J = 15,7 Hz, CH_3-CH_2), 7.36–7.82 (m, j = 7.9, 7.86, 8.3 Hz, 4H_{Ar}); ^{13}C NMR (DMSO d_6) δppm: 13.87 (CH_3-CH_2); 21.01 ($CH_{3,quin}$); 62.04 (CH_2-N_{Quin}); 62.38 (CH_2-CH_3); 154.28 ($C_{,amide\ tert}$); 157.28 (C_{ester}) 160.27 (C_{amide}). HRMS (ESI-MS) (m/z) calculated for $C_{18}H_{20}N_4O_6$ 388,14 found 389.14597 (positifs) 387.13101 (negatifs)

The synthesis of the compound MQOAHM is depicted in Scheme1. The starting material, 3-methylquinoxalin-2(1H)-one was prepared through treatment of *o*-phenylenediamine with sodium pyruvate in acetic acid (Hinsberg, 1887). This heteroycle was proven to be a good synthon for different highly biologically active compounds. The lactam function of quinoxalinone is very reactive, and so it was condensed with ethyl 2-bromoacetate to obtain the alkylated compound EMQOA. This intermediate reacts with hydrazine to form the corresponding hydrazide MQOAH. The condensation of this hydrazide with diethyl 2-oxomalonate allowed us to isolate the title compound MQOAHM. The structure of MQOAHM was elucidated based on spectral data.

The ^{1}H NMR spectrum revealed three signals at δ 2.48, 5.41 and 12.64 ppm due to the methyl group, CH_2 attached to the quinoxaline nitrogen and the NH of acetamide group, respectively. Also, ^{1}H NMR shows a triplet at δ 1.29 ppm and quadruplet at δ 4.34 ppm corresponding to two ethyls of the malonate. This confirms the reaction between MQOAH and diethyl-2-oxomalonate. ^{13}C NMR spectrum showed signals at δ 13.61, 21.01, 62.04, 154.28 and 160.27 ppm referring to the methyl group and CH_2 attached to quinoxaline nitrogen group, C═N of quinoxaline group, C═O of quinoxaline group and carbon of acetamide group respectively (Missioui et al., 2021). The remaining signals are, δ 122.13 (C═N), 157.28 (C═O) and 13.87, 62.68 (CH_2-CH_3). The IR spectrum of MQOAHM showed bands at 3215, 1655 and 1733 cm^{-1} for the NH, carbonyl and ester groups, respectively. The spectral data were in agreement with its structure.

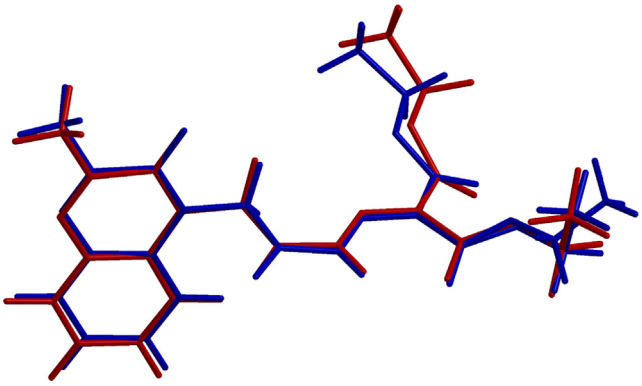

Fig. 5 Superposition of experimental structure (blue) and theoretical structure (red) (RMS = 0.254 Å).

3.2. Crystal description and optimized molecular structure

The quinoxaline moiety, except N2, is planar to within 0.0169 (15) Å (rms deviation = 0.0098). N2 is displaced by 0.0307(18) Å from the mean plane. The attached substituent to N2 is nearly perpendicular to the mean plane defined above as indicated by the dihedral angle of 83.34(6)° between this plane and that defined by N2/C11/C12/O2. The intramolecular N3─H3A···O5 hydrogen bond (Table 2) orients, the two ester groups to be close to coplanarity with the N2/C11/C12/O2 unit (Fig. 3). Bond distances and interbond angles appear as expected for the given formulation. In the crystal, slipped π-stacking interactions between C1···C6 and C1/C6/N1/C7/C8/N2 rings (centroid···centroid = 3.6768(11)Å, dihedral

Table 3 Experimental and theoretical bond distances of the title compound (Å).

Bond Distances							
Atoms	X-ray	DFT	Error	Atoms	X-ray	DFT	Error
O1-C8	1.227(2)	1.2241	0.0029	N3-C11	1.379(2)	1.3952	−0.0162
O2-C11	1.203(2)	1.2068	−0.0038	N4-C12	1.284(2)	1.2917	−0.0077
O3-C13	1.200(2)	1.2068	−0.0068	C1-C2	1.391(3)	1.4033	−0.0123
O4-C13	1.331(2)	1.3381	−0.0071	C1-C6	1.409(2)	1.4139	−0.0049
O4-C14	1.453(2)	1.4538	−0.0008	C2-C3	1.367(3)	1.3876	−0.0206
O5-C16	1.209(2)	1.2191	−0.0101	C3-C4	1.394(3)	1.3997	−0.0057
O6-C16	1.382(12)	1.329	0.0530	C4-C5	1.369(3)	1.3837	−0.0147
O6-C17	1.458(3)	1.4579	0.0001	C5-C6	1.393(3)	1.4036	−0.0106
O6A-C16	1.264(18)	–	–	C7-C8	1.482(2)	1.4865	−0.0045
O6A-C17A	1.458(3)	–	–	C7-C9	1.492(3)	1.4973	−0.0053
N1-C6	1.386(2)	1.3839	0.0021	C10-C11	1.514(2)	1.5296	−0.0156
N1-C7	1.288(2)	1.2907	−0.0027	C12-C13	1.502(2)	1.5062	−0.0042
N2-C1	1.392(2)	1.3946	−0.0026	C12-C16	1.496(2)	1.4949	0.0011
N2-C8	1.374(2)	1.3931	−0.0191	C14-C15	1.480(3)	1.514	−0.0340
N2-C10	1.462(2)	1.4532	0.0088	C17-C18	1.483(4)	1.5182	−0.0352
N3-N4	1.3437(19)	1.3309	0.0128	C17A-C18A	1.483(4)	–	–

Table 4 The experimental and theoretical bond angles of the title compound (°).

Atoms	X-ray	DFT	Atoms	X-ray	DFT
C13-O4-C14	115.92(14)	116.2714	O1-C8-N2	122.30(16)	121.924
C16-O6-C17	115.7(8)	117.8383	O1-C8-C7	122.21(17)	122.7191
C16-O6A-C17A	116.9(12)	–	N2-C8-C7	115.48(16)	115.3488
C7-N1-C6	119.27(15)	119.5245	N2-C10-C11	111.38(14)	111.596
C8-N2-C1	122.25(14)	121.9489	O2-C11-N3	120.32(15)	119.9901
C1-N2-C10	120.19(15)	121.5005	O2-C11-C10	123.93(15)	124.4707
C8-N2-C10	117.53(15)	116.5303	N3-C11-C10	115.74(14)	115.5345
N4-N3-C11	117.11(13)	120.4597	N4-C12-C13	114.03(14)	116.06
C12-N4-N3	121.99(14)	122.0905	N4-C12-C16	124.41(15)	123.9618
C2-C1-N2	123.00(15)	122.9902	C16-C12-C13	121.54(14)	119.9065
C2-C1-C6	119.32(16)	119.3372	O3-C13-O4	124.44(16)	124.9546
N2-C1-C6	117.67(16)	117.6719	O3-C13-C12	124.88(16)	122.9788
C3-C2-C1	120.14(17)	119.9963	O4-C13-C12	110.67(14)	112.0462
C2-C3-C4	121.11(18)	120.9501	O4-C14-C15	106.13(17)	107.5125
C5-C4-C3	119.25(18)	119.3938	O5-C16-O6A	122.9(5)	–
C4-C5-C6	121.02(17)	120.8274	O5-C16-O6	126.6(4)	124.623
N1-C6-C1	121.82(16)	122.1115	O5-C16-C12	122.94(15)	122.8051
N1-C6-C5	119.00(15)	118.3985	O6A-C16-C12	112.9(5)	–
C5-C6-C1	119.15(16)	119.489	O6-C16-C12	110.4(3)	112.5148
N1-C7-C8	123.41(16)	123.34	O6-C17-C18	108.6(5)	111.1413
N1-C7-C9	120.31(16)	120.4127	O6A-C17A-C18A	108.6(9)	–
C8-C7-C9	116.27(16)	116.2473			

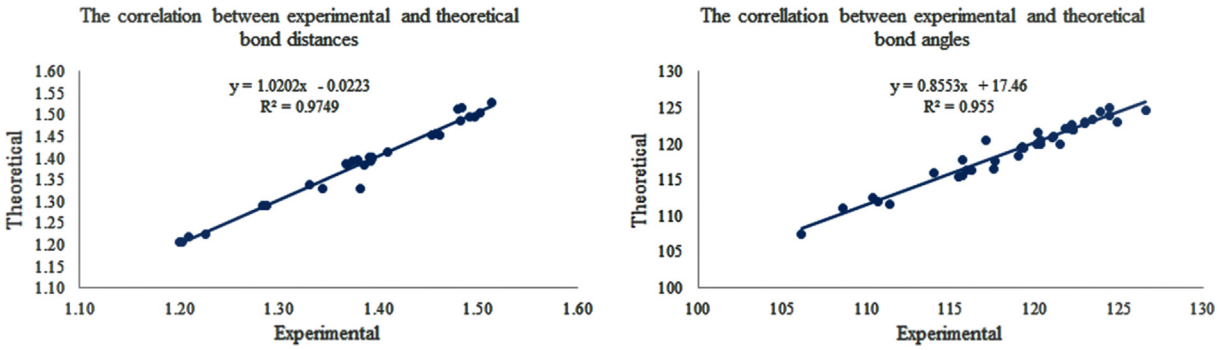

Fig. 6 The correlation values between experimental and theoretical geometrical parameters.

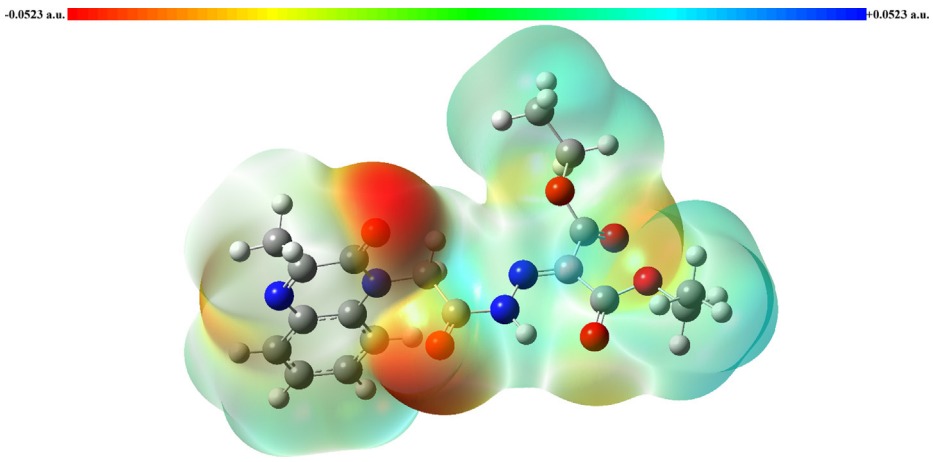

Fig. 7 The Molecular Electrostatic Potential map of the molecule.

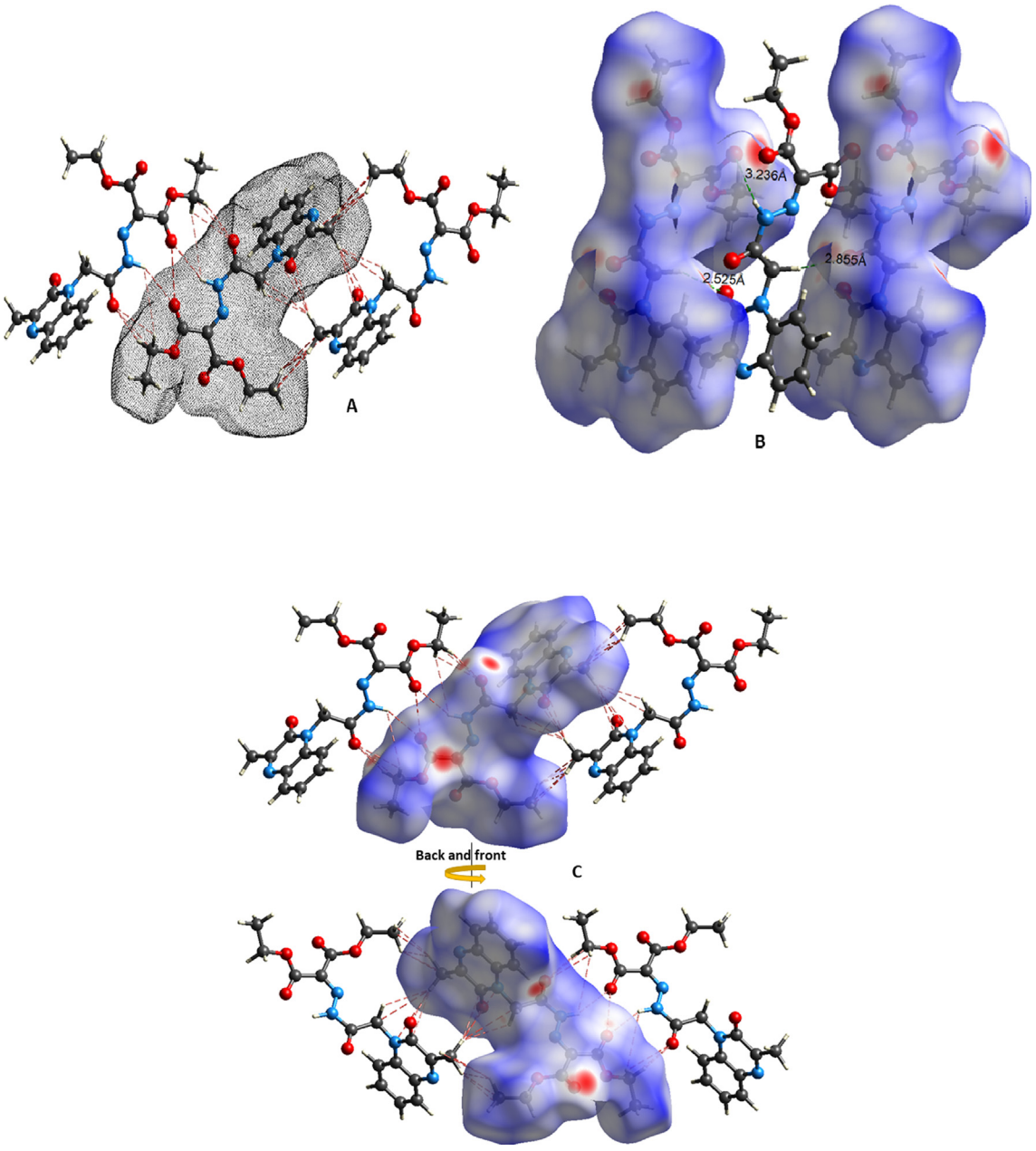

Fig. 8 (A) A mesh presentation of the **MQOAHM (a)** packing showing the electron density around all the molecule atoms using the Crystal Explorer software and CIF data. H-bonds are presented using red dashed lines; (B) The HSA d_{norm} map of both sides of the molecule. Blue areas indicate low-intensity contacts and red areas indicate high-intensity contacts. N-H. . .O and C-H. . .H-C interactions are also shown.

angle = 0.89(9)°, slippage = 1.53 Å), together with C2—H2···O2 and C10—H10B···O1 hydrogen bonds plus C9—H9A···Cg1 interactions (Table 2) form oblique stacks of molecules extending along the *a*-axis direction (Fig. 2). These stacks are connected in pairs by inversion-related C17—H17B···O2 hydrogen bonds (Table 2 **and** Fig. 4).

3.3. Computational studies

3.3.1. Geometric optimization of the compound

The optimized geometry of diethyl 2-(2-(2-(3-methyl-2-oxoquinoxalin-1(2H)-yl)acetyl)hydrazono)malonate molecule was obtained by DFT/B3LYP, 6–311 + + G(d,p) method. Due to disorder at one of methoxyethane groups, the theoretical structure was found by choosing O6-C17-C18 state of methoxyethane group. The superimposition of the theoretical and experimental structures can be seen in Fig. 5. Although the ethyl acetate groups of the molecule don't overlap, theoretical and experimental structures almost overlap on each other for the other part. After calculation, the minimum energy of the molecule was calculated as −1368.7186 a.u.

Bond distances and bond angles in both X-ray results and theoretical results are given in Table 3 and Table 4, respectively. Linear correlations for all bond distances and all bond

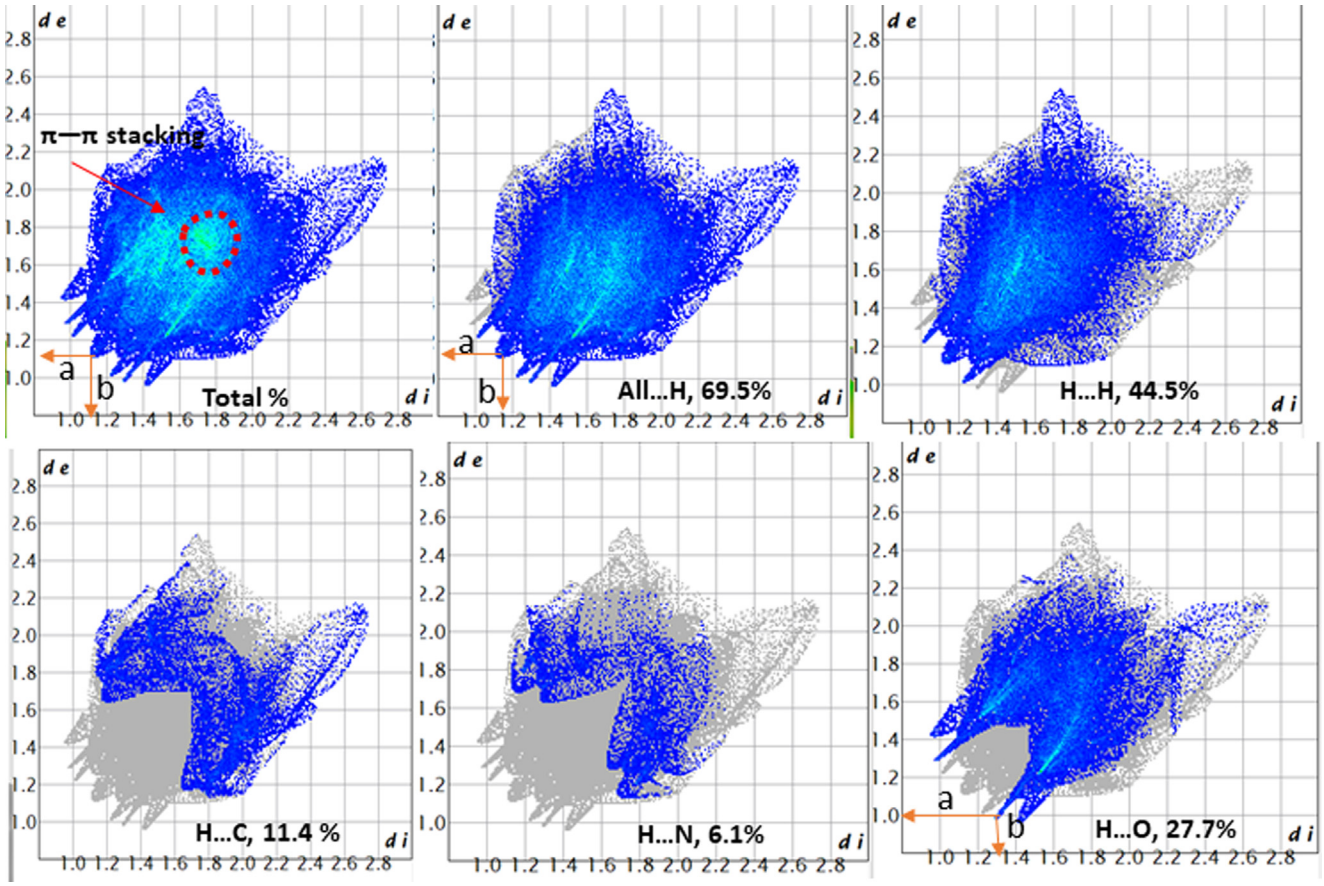

Fig. 9 Hirshfeld surface fingerprint plots of the nearest external distance (a = d_e) for **MQOAHM (a)** versus the closest internal distance (b = d_i). The d_i and d_e refer to intra- and intermolecular contacts, respectively.

angles are shown in Fig. 6, too. In addition, the theoretical bond distances are close to the experimental bond distances. The most significant difference between theoretical and experimental bond distance was calculated for O6—C16 with 0.0530 Å error. The theoretical result of the O6—C17 is closest to the experimental result. RMSE and R^2 values were computed a 0.0162 Å, 0.9749 for all bond distances, respectively.

The most significant difference between theoretical and experimental bond angles is 3.3497° for N4—N3—C11 bond angle. RMSE and R^2 values for bond angles were found at 1.1314° and 0.955. If the bond angles were compared with the bond distances, the theoretical bond angles deviate further than the experimental bond angles with respect to bond distances.

The N2—C10—C11—N3, C10—C11—N3—N4 and C11—N3—N4—C12 torsion angles obtained X-ray diffraction are 173.10(15)°, −1.6(2)° and 174.97(15)°, respectively. Theoretical results of these torsion angles are 176.8909°, −1.8020° and 178.4503°, respectively.

3.3.2. Molecular Electrostatic map

Molecular Electrostatic Potential (MEP) map gives valuable information about intermolecular interactions. DFT method, B3LYP functional with 6–311 + + G (d,p) basis set, was set to create the MEP of this molecule. MEP contains blue and red areas, showing nucleophilic attack centres. Red regions show electrophilic attack centres. The most electrophilic attack centres for the molecule were calculated around the oxygen and N1 atoms. These regions can be seen in Fig. 7**.** Charge values for these regions are −0.05223 a.u. for O1, −0.04888 a.u. for O2, −0.04146 a.u. for O3, −0.02732 a.u. for O5 and −0.03642 a.u. for N1 atom. According to X-ray diffraction, the crystal structure has intermolecular C2—H2···O2, C10—*H*10···BO1 and C17—H17B···O2 hydrogen bonds. From these results, MEP is compatible with x-ray results.

3.3.3. Hirshfeld surface analysis

HSA is a successful tool in showing the inter-and intramolecular interactions in the crystal structure. The mesh drawing generated using Crystal Explorer shows the electron density around all of the molecule atoms and displays the short contacts, within 3.8 A° in red dashed lines, Fig. 8**(A)**, (Trott and Olson, 2009). Many types of these interactions were detected (N---H. . .O, C---H. . .C, C---H. . .O and more) as red spots on the ligand surfaces Fig. 8**(B), (C)**. This agrees with the bonding interactions found by X-ray structure analysis. The red spots represent the points of closest interactions, whereas the blue areas show weak interactions. Also, HSA was employed in this study to show the d_e and d_i for **MQOAHM (a),** Fig. 9. Because **MQOAHM (a)** has many heteroatoms (6O and 4N) and polar H atoms, it was expected to reveal several red spots on the computed surface, Fig. 8**(B), (C)** (Özdemir Tarı et al., 2018; Asadi et al., 2017). Combining the d_e and d_i on a fingerprint plot proposes helpful information about all the contacts in the molecule. The intermolecular interactions, N—H. . .O, C—H. . .H, C—H. . .C and C—H. . .N,

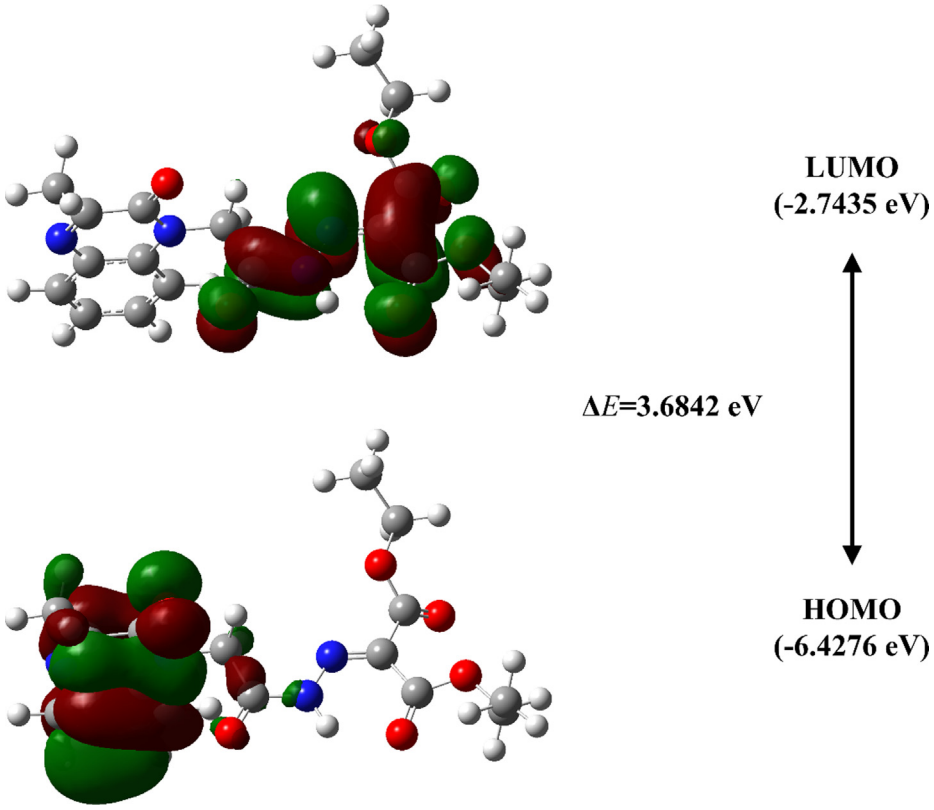

Fig. 10 Highest Occupied Molecular Orbital (HOMO) and Lowest Unoccupied Molecular Orbital (LUMO) orbitals with the energy gap.

provide the stabilized molecular packing. These interactions are responsible for holding the molecules in layers in the crystal packing. The H...H contacts, in the fingerprint plots, show a high percentage of the interactions in **MQOAHM (a),** (44.5%). The second highest interaction is O...H (27.7%). The third is C...H, which displays 11.4%. The spikes due to the H...O contacts are apart on the fingerprint plots ($d_e + d_i$) 2.3 Å, corresponding to 27.7% of all O...H interactions. The red dashed circle on d_{norm} Hirshfeld surface shows the presence of π-π stacking, which corresponds to the phenyl–phenyl interaction. All 2D-finger plots and the percentage contributions of many interactions are shown in Fig. 9.

Table 5 Main protease with various resolutions.

Protease	Resolution	Inhibitor	PDB number
7BQY	*1.70 Å*	*N3*	*https://doi.org/10.2210/pdb7BQY/pdb*
7C8U	2.35 Å	MPI5	https://doi.org/10.2210/pdb7C8U/pdb
7JQ2	1.4 Å	MPI5	https://doi.org/10.2210/pdb7JQ2/pdb
7BUY	1.6 Å	carmofur	https://doi.org/10.2210/pdb7BUY/pdb
6M0K	1.50 Å	11b	https://doi.org/10.2210/pdb6M0K/pdb
5R81	1.95 Å	Z1367324110	https://doi.org/10.2210/pdb5R81/pdb
5R82	1.31 Å	Z219104216	https://doi.org/10.2210/pdb5R82/pdb
6LU7	2.16 Å	inhibitorN3	https://doi.org/10.2210/pdb6LU7/pdb
5R7Y	1.65 Å	Z45617795	https://doi.org/10.2210/pdb5R7Y/pdb
5R7Z	1.59 Å	Z1220452176	https://doi.org/10.2210/pdb5R7Z/pdb
5R80	1.93 Å	Z18197050	https://doi.org/10.2210/pdb5R80/pdb

3.3.4. Frotier molecular orbitals

Highest Occupied Molecular Orbital (HOMO) and Lowest Unoccupied Molecular Orbital (LUMO), which are called Frontier Molecular Orbitals (FMOs) because of laying at the outermost boundaries, are very important to explain photostability and molecular transport properties (Prasad and Ojha, 2017). While Highest Occupied Molecular Orbital (HOMO) is related to ionization potential, and Lowest Unoccupied Molecular Orbital (LUMO) is related to electron affinity. The energy gap between HOMO and LUMO is related to charge transfer in molecules (Nataraj et al., 2012) and identifies the chemical stabilities of molecules (Gilman, 2007). Furthermore, a low energy gap indicates high biological activity due to transferring electrons efficiently from HOMO (Wu et al., 2020). Additionally, average energy values for HOMO and LUMO are connected to electronegativity (Prasad and Ojha, 2017). HOMO and LUMO of the molecule were plotted using the same level theory. These Frontier Molecular Orbitals

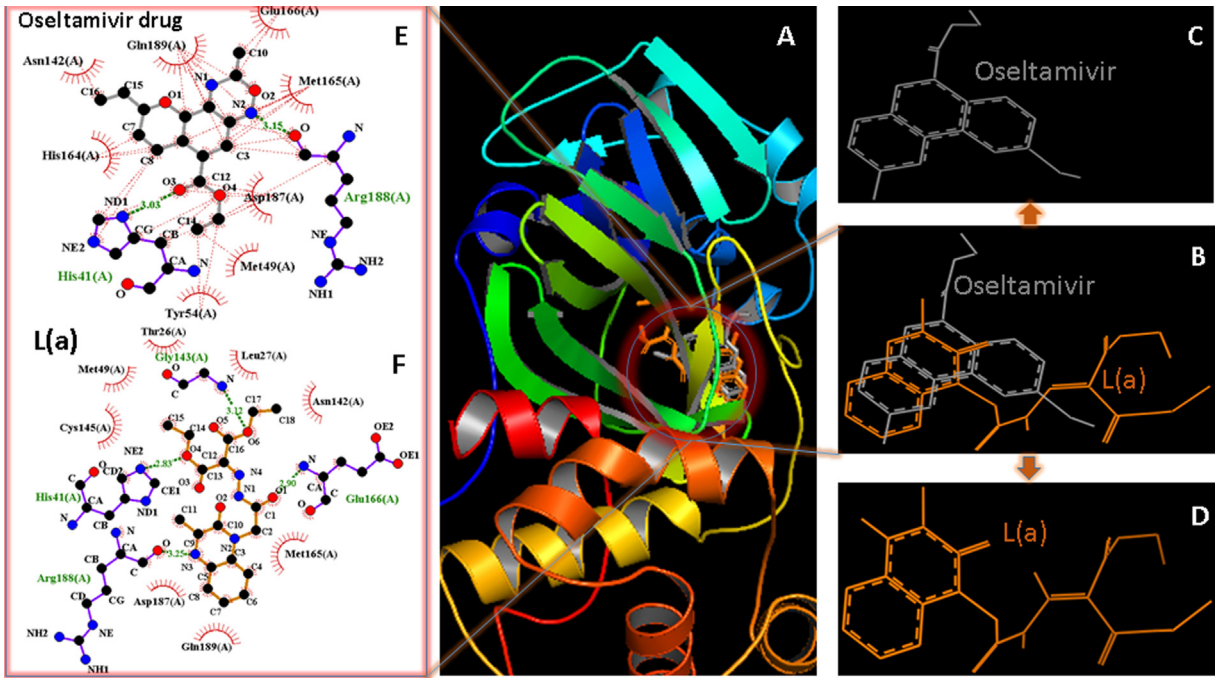

Fig. 11 (A) The superposition of our ligand **MQOAHM (a)** and Oseltamivir-approved drug docked to**7BQY** using the same parameters for a fair comparison. All ligands are colour-coded. Results are presented using PyMOL (DeLano, 2004); (B) The superposition of our ligand **MQOAHM (a)** and Oseltamivir without **7BQY** for clarity; (C) The display of Oseltamivir approved drug alone; (D) The display of **MQOAHM (a)** alone; (E and F) A schematic 2D LIGPLOT representation of Oseltamivir (grey lines) and **MQOAHM (a)** (orange lines) against **7BQY** complex showing the hydrogen and hydrophobic interactions in (E) and only H-bonds in (F). A key to the symbols is given in our recent report (Alsafi et al., 2020). Schematic 2D LIGPLOT representations of all molecules are available in the SI.

(FMOs) and the energy gap between HOMO and LUMO can be seen in Fig. 10. While HOMO orbital is mainly localized on 3-methylquinoxalin-2(1H)-one molecule group, LUMO orbital is mainly localized on diethyl 2-(2-acetylhydrazono)malonate group. The energy gap between HOMO and LUMO is 3.6842 eV.

3.4. Docking analysis against 7BQY

The whole world is experiencing a tough time at many economic and social levels because of Covid-19. Hence, we have been motivated to study how a malonate ligand might behave in the main protease's active site for Covid-19 (M^{Pro}, PDB 7BQY). Worth mentioning that previous docking studies have used the main protease, M^{pro}, Table 5, with different resolutions (Vraj Shah and Bhaliya, 2020). In this study, we preferred to use the 7BQY because it has been docked against the well-known inhibitor N3 that appeared recently in *Nature journal* and has a good resolution value (1.70 Å) (Jin et al., 2020). All the collected proteases in Table 5 can be used in docking as they are around 2 Å in resolution (https://www.rcsb.org/).

The newly formed H-bonding and hydrophobic interactions between the ligand and the protein binding site due to docking directly affect the ligand's structural reorganization and 7BQY. For example, our single-crystal X-ray study of N4-N3-C11-C10 and C13-C12-C16-O6 of L(a) found the torsion angles in our single-crystal X-ray study before docking is −1.55 and 8.21°. In contrast, the torsion angles after docking for the same are −3.84 and 18.82°, respectively. This indicates that varying degrees of adjustment of the ligand upon binding with the main protease for COVID-19 (M^{pro}; PDB code 7BQY) for a better fit in the site has taken place (Alsafi et al., 2020). A representative example of a superposition of **MQOAHM (a)** (orange lines) and Oseltamivir (approved drug by FDA, grey lines) docked against 7BQY using the same parameters for a fair comparison is shown in Fig. 11. The superposition reveals an overlap between the two molecules in the site of the protease.

Furthermore, the binding energy of **MQOAHM (a)** and Oseltamivir are −7.0 and −7.5 kcal/mol, respectively, indicating possible similar biological activities between the two molecules. Results may suggest further study of the **MQOAHM (a)** in the context of a potential drug for the coronavirus, Table 5. Likewise, **MQOAHM (a)** was superposed on 18 approved drugs (Shah et al., 2020); **N3** (Jin et al., 2020) and **MQOAHM (b)** to reveal a highly interestingly wider range of displays of the compounds bound to the protein cavity of 7BQY compared to **MQOAHM (a)**. All molecules are colour-coded throughout the study, Fig. 12. The reason for choosing these approved drugs is that they are active against different viral diseases (Ebola virus, HI, Herpes, Hepatitis, Influenza, Cytomegalovirus, Small Pox and more) (Shah et al., 2020; Lagunin et al., 2018). The result revealed that the studied malonate-based ligand **MQOAHM (a)** has a similar layout and binding affinity, against the main protease (PDB code 7BQY), to the 18 approved drugs and **N3** inhibitor, Fig. 12.

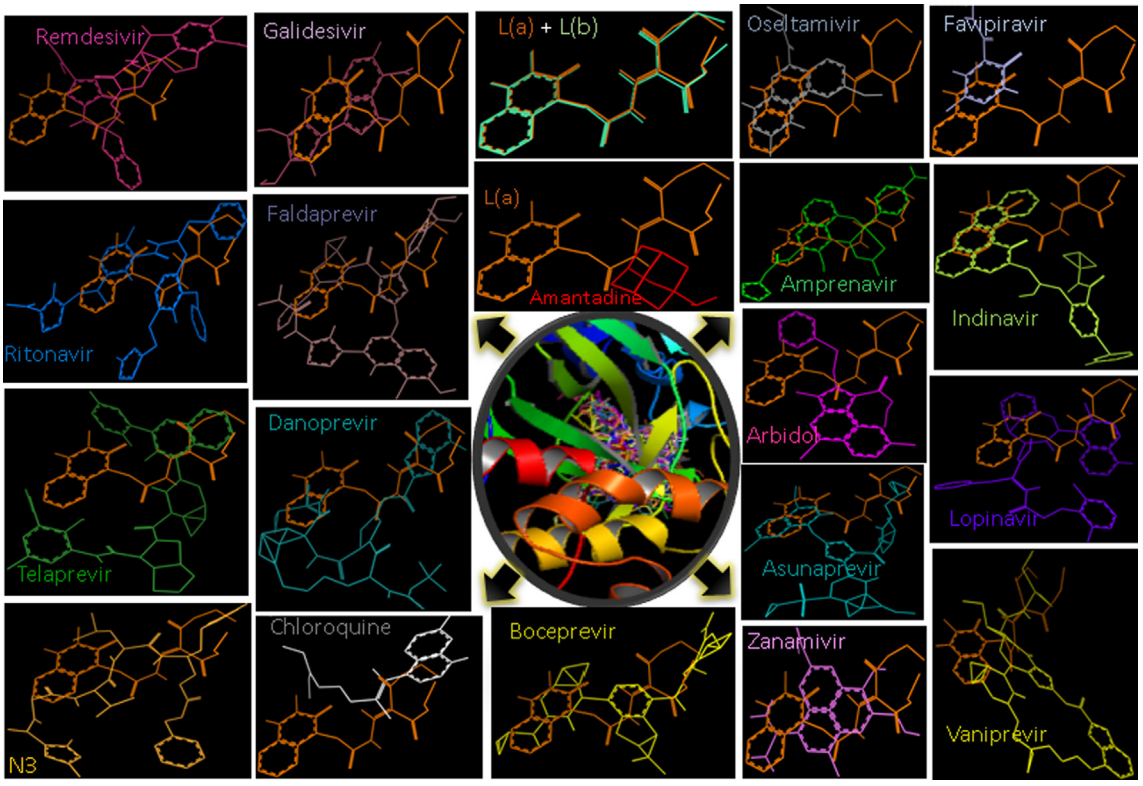

Fig. 12 The superposition of 18 approved drugs, N3, and **MQOAHM (a), (b)** docked together into the binding pocket of **7BQY** using the same parameters for a fair comparative study. The results are represented by PyMOL (DeLano, 2004) in the circle frame. Every docked drug is shown separately in a rectangular frame alongside our ligand **MQOAHM (a)** (orange stick). All are colour-coded. The top middle rectangular shows a superposition of our disordered independent molecules, **MQOAHM (a)** and **MQOAHM (b)**.

It is essential to mention that all the docked molecules against the target enzyme COVID-19 are ranked according to their binding energy, shown in ascending order and colour-coded molecules (Fig. 13). The binding affinity was attributed to many hydrogen bonds and hydrophobic interactions between the **MQOAHM (a)** and the receptor's active amino acid residues, as shown in the Schematic 2D LIGPLOT, Fig. 11 **(F)**. A similar full Schematic 2D LIGPLOT for Oseltamivir was presented for comparison, Fig. 11 **(E)**. It could be seen that Arg188(A) and His 41(A) are the two common amino acids responsible for the hydrogen bond formation in both compounds. Docking of the disordered independent molecules MQOAHM (a) and MQOAHM (b) has been performed alongside the 18 drugs and N3 in one go and under the same conditions to make it a fair comparison. The docking result of **MQOAHM (a)** can be compared to **MQOAHM (b)** to show a slight difference in the layout of the aliphatic part of the ligand but a similar layout in the aromatic part in the binding site of the protease, Fig. 12**, MQOAHM (a) + MQOAHM (b).**

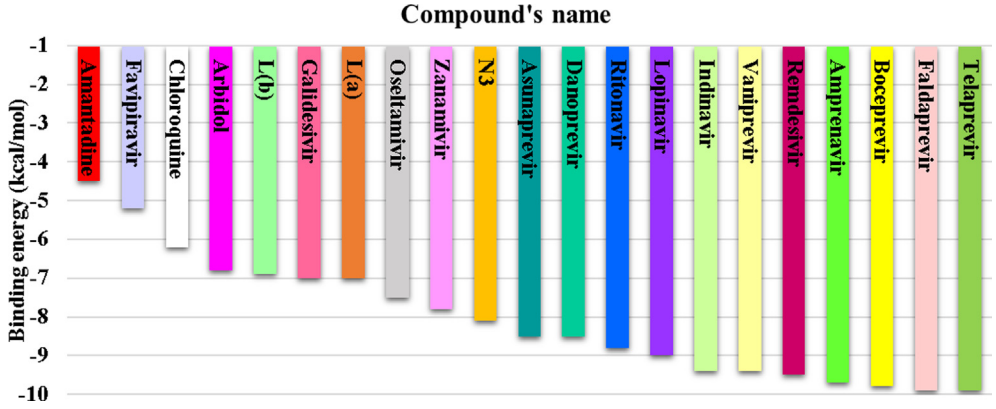

Fig. 13 Binding affinities of **MQOAHM (a)**, **MQOAHM (b)**,18 approved drugs and the inhibitor **N3** against COVID-19, 7BQY protease.

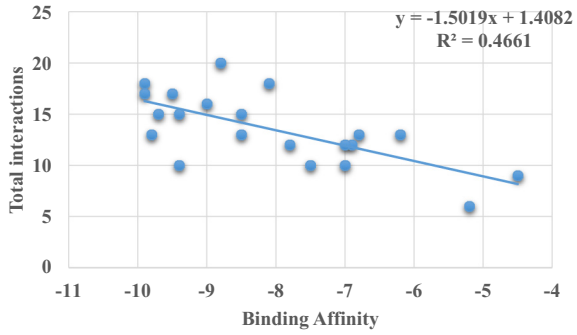

Fig. 14 Binding affinities against the total number of interactions for **N3**, **MQOAHM (a)**, **MQOAHM (b)** and the 18 approved drugs.

Essential roles in identifying effective drugs for COVI-19 are the protein-drug complexes and binding affinity; therefore, M^{pro} is well assigned to serve as the key drug target (Bhatia et al., 2020). Molecular docking computations in this study showed that **MQOAHM (a)** and **MQOAHM (b)** have a good binding affinity to the SARS-CoV-2 main protease (M^{pro}) in comparison to all the approved drugs. In fact, what is interesting about the data in Fig. 15 is that **MQOAHM (a)** and **MQOAHM (b)** were docked against 7BQY alongside 18 approved drugs and **N3** inhibitor, in one run. The same parameters and conditions were used to rank our ligand compared to a large number of the approved drugs and **N3** inhibitor used here. The range of the binding affinities of the 18 drugs in this study and **N3** is from −4.5 to −9.0 kcal/mol, whereas the binding affinities of **MQOAHM (a)** and **MQOAHM (b)** are −7.0 and −6.9 kcal/mol, respectively. Thus the ligands are one unit less kcal/mol than the average value of all compounds, − 8.0 7 ± 1.56 kcal/mol, Fig. 13. Besides, **MQOAHM (a)** and **MQOAHM (b)** demonstrated closer binding modes inside the active site of M^{pro}, establishing crucial hydrogen bonds and hydrophobic interactions with various amino acid residues, Fig. 11 and **SI**. The similar behavior of **MQOAHM** compared to the rest of the molecules in this study, suggest that our ligand merit considering in the context of a possible therapeutic agent for COVID-19, Fig. 12**,** Fig. 13. A quick check of each molecule's total interactions with the binding site was performed by counting the total number of hydrogen and hydrophobic interactions. Interestingly, the statistical analysis supports that as the number of interactions increases, the binding energy gets lower (more negative, better) to a reasonable extent, Fig. 14. There are 47 Hydrogen bonds and 237 hydrophobic interactions for all the molecules involved in this study Fig. 15 (**SI**).

H-bonds and hydrophobic interactions emerged upon docking all the molecules used in this study to the substrate-binding pocket of COVID-19 (7BQY protease), summarised in Fig. 15. Amino acid E166 was responsible for creating the highest total number of H-bonds and hydrophobic interactions. Amino acid E166 forms an almost equal number of hydrophobic and hydrogen interactions. Amino acids T24 and S46 show only hydrogen bonds, whereas T25, F140, M165, L167, P168, H172 and D187 show only hydrophobic interactions.

The binding affinity to the protein target is usually considered in selecting a possible drug candidate. All docking poses demonstrated a good fit inside the substrate pocket. Therefore, the lowest-energy docking poses of all compounds were considered for the superposition in Fig. 12. Analysis results for all the nine poses of each molecule docked to 7BQY are presented in Table 6 to assess the predicted binding poses' reasonability. Statistical analysis, using a statistical model (Minitab Statistical Software (Version 19) 2020. Available from: www.minitab.com), showed no significant differences between the nine-poses for each compound used, Table 5**-SI**. However, a highly significant variation between the nine-poses and compounds' binding affinity means at p-value = 0.00, Table 6. The Pairwise comparison, Tukey, showed that Telaprevir with a mean of −9.20 ± 0.36 is the strongest significant binding affinity. The following medicines have no significant differences in their M^{pro} binding affinity; Faldaprevir (−9.06 ± 0. 38), Indinavir (−8.94 ± 0.29), Remdesivir (−8.80 ± 0.39) and Telaprevir (−9.20 ± 0.36), Table 6**,** Table 7**-SI**. The drugs Boceprevir, Lopinavir, Vaniprevir, Amprenavir, Ritonavir, and Asunaprevir have a binding affinity (−8.50 to −8.1), Table 6**,** Table 7**-SI**. **MQOAHM (a)** and **MQOAHM (b)** have (−6.67 ± 0.22) and (−6.63 ± 0.18) binding affinity, respectively. **MQOAHM (a)** and **MQOAHM (b)** show no significant differences when compare to other drugs; Oseltamivir (−6.78 ± 0.42) and Arbidol (−6.43 ± 0.18). The lowest binding

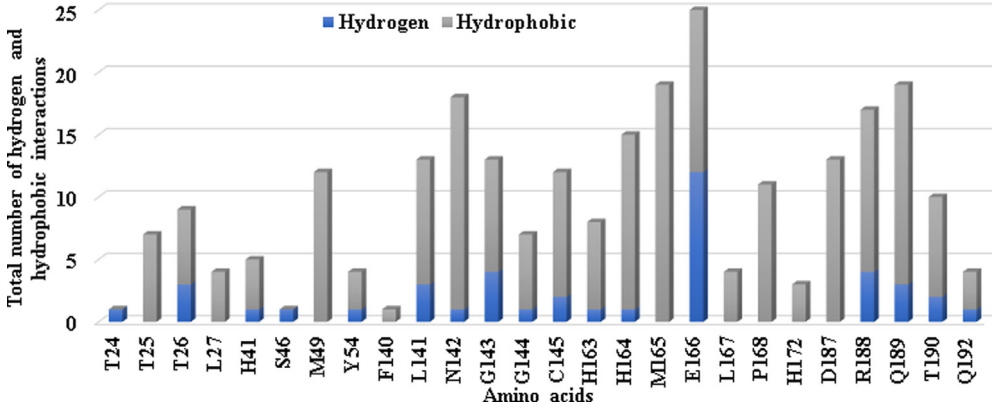

Fig. 15 Total number of H-bonds and hydrophobic interactions emerged upon docking all the molecules to 7BQY protease.

Table 6 Poses Binding affinities mean and StDev of all compounds against COVID-19, 7BQY. Pooled StDev = 0.377894. Means that do not share a letter are significantly different.

Compound	Mean ± StDev	Compound	Mean ± StDev
Amantadine	−4.22 ± 0.17^{a}	Ritonavir	−8.14 ± 0.26 ^{g}
Favipiravir	−4.85 ± 0.22^{a}	Asunaprevir	−8.17 ± 0.28^{gh}
Chloroquine	−5.88 ± 0.22^{b}	Amprenavir	−8.36 ± 0.69^{ghi}
Galidesivir	−6.28 ± 0.31^{bc}	Vaniprevir	−8.44 ± 0.63^{ghij}
Arbidol	−6.43 ± 0.18^{bc}	Lopinavir	−8.47 ± 0.36^{ghij}
MQOAHM (b)	−6.63 ± 0.18 ^{cd}	Boceprevir	−8.50 ± 0.72^{ghij}
MQOAHM (a)	−6.67 ± 0.22 ^{cd}	Remdesivir	−8.80 ± 0.39^{hijk}
Oseltamivir	−6.78 ± 0.42^{cde}	Indinavir	−8.94 ± 0.29^{ijk}
Favipiravir	−7.22 ± 0.24^{de}	Faldaprevir	−9.06 ± 0.36^{jk}
N3	−7.41 ± 0.29^{ef}	Telaprevir	−9.20 ± 0.36 ^{k}
Danoprevir	−7.91 ± 0.33 ^{fg}		

Table 7 Possible biological activity of the title compound using PASS at Pa > Pi.

Biological activities on tumor cell-line	Pa	Pi
Antieczematic	0.616	0.079
Antiviral (Picornavirus)	0.524	0.041
Mediator release inhibitor	0.431	0.029
Antituberculosic	0.418	0.026
Platelet aggregation stimulant	0.472	0.087
Trimethylamine-oxide aldolase inhibitor	0.427	0.066
Proteasome ATPase inhibitor	0.453	0.094
Cyclic AMP phosphodiesterase inhibitor	0.405	0.056
ATPase stimulant	0.346	0.011

Table 8 Predicted adverse and toxic effect by the title compound using PASS at Pa > Pi.

Predict adverse and toxic biological activities	Pa	Pi
Twitching	0.531	0.184
Edema	0.367	0.150
Splenomegaly	0.285	0.182
Telangiectasia	0.148	0.100
Gastrointestinal hemorrhage	0.277	0.250

affinity means calculated for Chloroquine, Amantadine, and Favipiravir nine-poses have (−5.88 ± 0.22), (−4.22 ± 0.17) and (−4.85 ± 0.22), respectively Table 6, Table 7-**SI**.

3.5. PASS and Way2drug (Prediction of biological and cytotoxicity activities)

PASS (Prediction of Activity Spectra) (Lagunin et al., 2000) and Way2drug (Provides more information about the biological potential of new compounds, Way2Drug URL, http://way2drug.com) (Druzhilovskiy et al., 2017) are online software tools that predict various types of biological activities as shown in Table 7. They were both used at Pa > Pi (Pa represents the probability of being active, and Pi means inactive).

Table 9 Predicted cytotoxic of title compound on tumor cell lines using Drug-2Way at Pa > Pi.

Cell line	Tumor cell-line full name/(tissue)	Pa	Pi
MDA-MB-453	Breast adenocarcinomal/(Breast)	0.468	0.018
YAPC	Pancreatic carcinoma/(Pancreas)	0.379	0.131
U-937	Histiocytic lymphoma/ ((Haematopoietic and lymphoid tissue)	0.300	0.016
MDA-MB-361	Breast adenocarcinoma/(Breast)	0.257	0.056
C8166	Leukemic T-cells/(Breast)	0.274	0.135

Table 10 Predicted cytotoxic of title compound on non-tumor cell lines using Drug-2Way at Pa > Pi.

Cell line	Non-tumor Cell-line full name and tissue name	Pa	Pi
CRL-7065	Fibroblast (Skin)	0.092	0.055
AG1523	Fibroblast (Fibroblast)	0.043	0.032

The aim mainly was to predict the cytotoxicity of our malonate-based ligand **MQOAHM (a)** against human tumours and non-tumours. The first predicted biological activity for **MQOAHM (a)** was Antieczematic, ranging from 0.079 to 0.616. Whereas, the second predicated activity was antiviral against a single-stranded RNA Picornavirus. This virus is considered a simple and positive-sense RNA vertebrate virus group. It comprises many small RNA viruses that cause significant pathogens in both humans and livestock (Abramo et al., 2012). The activity predicated, by PASS, was in the range of 0.041–0.524. The Picornaviruses (PV) and coronaviruses (Cov), to which COVID-19 belongs, are positive-stranded RNA viruses that infect humans worldwide. Around 6800 small molecules were tested to discover a novel inhibitor against viral protease for both viruses. Results showed a protease that inhibits SARS-CoV 3CL^{pro} and 3C^{pro} from PV and CoV, respectively (Kuo et al., 2009). Therefore, in this study, **MQOAHM (a)** and **MQOAHM (b)** were biologically docked to COVID-19 M^{pro} alongside a range of approved antiviral drugs for comparison. Other inhibiting activities predicated by PASS are Mediator release, Trimethylamine-oxide aldolase, Proteasome ATPase, and Cyclic AMP phosphodiesterase inhibitors. Stimulant activity for **MQOAHM (a)** predicated by PASS as Platelet aggregation and ATPase, Table 7. Side negative effect was also predicted, such as

Muscle twitching, oedema, splenomegaly, telangiectasia and Gastrointestinal Haemorrhage with Pa starting from 0.531 as a higher value and 0.277 as a lower value Pa, Table 8. **MQOAHM (a)** was tested using Drug2Way

for three cell lines from breast tissues; MDA-MB-453, MDA-MB-361 and Leukemic T-cells with Pa at 0.468, 0.257 and 0.274, respectively and Pi at 0.018, 0.056, and 0.135, respectively Table 9. Other cell lines also recorded YAPC and U-937 from Pancreatic Carcinoma and Histiocytic Lymphoma, respectively Table 10. Predicted adverse toxic biological activities found in two non-tumor, Fibroblast cell lines, CRL-7065 and AG1523, for skin and Fibroblast at lower activities 0.092 and 0.043, respectively.

Table 11 Calculated ADMET properties

Property	Value
Absorption	
Caco-2 Permeability	−5.095
MDCK Permeability	3.8e−05
Pgp-inhibitor	0.01
Pgp-substrate	0.001
HIA	0.007
$F_{20\%}$	0.888
$F_{30\%}$	0.972
Distribution	
PPB	95.23%
VD	0.411
BBB Penetration	0.647
Fu	2.994%
Metabolism	
CYP1A2 inhibitor	0.504
CYP1A2 substrate	0.817
CYP2C19 inhibitor	0.391
CYP2C19 substrate	0.169
CYP2C9 inhibitor	0.648
CYP2C9 substrate	0.104
CYP2D6 inhibitor	0.01
CYP2D6 substrate	0.06
CYP3A4 inhibitor	0.443
CYP3A4 substrate	0.54
Excretion	
CL	0.127
$T_{1/2}$	0.56
Toxicity	
hERG Blockers	0.401
H-HT	0.117
DILI	0.933
AMES Toxicity	0.017
Rat Oral Acute Toxicity	0.006
FDAMDD	0.017
Skin Sensitization	0.081
Carcinogen city	0.045
Eye corrosion	0.003
Eye irritation	0.065
Respiratory Toxicity	0.336
Bioconcentration Factors	0.948
IGC_{50}	3.191
$LC_{50}FM$	4.726
$LC_{50}DM$	4.169
Tox21 pathway	
NR-AR	0.005
NR-AR-LBD	0.209
NR-AhR	0.878
NR-Aromatase	0.079
NR-ER	0.233
NR-ER-LBD	0.036
NR-PPARgamma	0.961
SR-ARE	0.278
SR-ATAD5	0.146
SR-HSE	0.656
SR-MMP	0.211
SR-p53	0.958

3.6. Admet prediction

In silico assessment of absorption, distribution, metabolism, excretion and toxicity (ADMET) properties were also used. It is a fast method to screen compounds for their pharmacokinetics and pharmacodynamics properties. The toxicity risks and bioavailability of **MQOAHM** were predicted based on ADMET profile (Table 11). Results showed a good human intestinal absorption probability, a good Blood-Brain Barrier crossing and a high plasma protein binding percentage. In addition**,** it has a good excretion and optimal toxicity except for drug-induced liver injury. The prediction results also showed that no carcinogenic effects and no AMES toxicity were found.

4. Conclusion

The disordered structure of the novel diethyl 2-(2-(2-(3-methyl-2-oxoquinoxalin-1(2H)-yl)acetyl)hydrazono)malonate was established by XRD single crystal analysis in a ratio of 0.596 (3)/0.404(3). Two strong types of hydrogen bond (C—H···O and C—H···C) interactions were detected in this molecule. Density Functional Theory (DFT) method, B3LYP, 6–311 + + G(d,p) basis set was used to optimize the molecule. The obtained results of bond distances are more compatible with the experimental results, whereas bond angles are less. MEP and HSA show that the vicinity of oxygen atoms are active regions for intermolecular interactions. Additionally, the energy gap is 3.6842 eV. A comparative study of the two forms of the title compound was docked together with a wide range of approved drugs and the ligand **N3,** against 7BQY, under the same conditions. The binding scores −7.0 and −6.9 kcal/mol^{-1} for **MQOAHM (a)** and **MQOAHM (b),** respectively suggesting almost no difference. Also, both the forms show almost identical lay down of the structures, after docking, indicating that the disorder of the molecule, in this study, has no clear-cut effect. However, the multi-hydrogen bond and hydrophobic interactions between the ligand and the receptor's active amino acid residues merits further research in the context of possible therapeutic agents for COVID-19. The binding scores of all the molecules used in this study ranged from −9.9 to −4.5 kcal/mol^{-1}. Preliminary toxicity properties of **MQOAHM** were predicated for its possible potential use as an inhibitory drug against COVID-19 using energy-free methods.

CRediT authorship contribution statement

Mohcine Missioui: Investigation. **Musa A. Said:** Investigation, Software, Writing – original draft. **Güneş Demirtaş:** Investigation, Software. **Joel T. Mague:** Data curation, Formal analysis. **Ahlam Al-Sulami:** methodology. **Nadia S. Al-Kaff:** methodology. **Youssef Ramli:** Conceptualization, methodology, Supervision, Writing-Reviewing and Editing.

Declaration of Competing Interest

The authors of this manuscript declare that they have no known competing financial interests or personal relationships that could have appeared to influence the work reported in this paper.

Acknowledgements

The authors are grateful to Mohammed V University and Ondokuz Mayıs University Research Fund for financial sup-

port for this study. The support of NSF-MRI Grant #1228232 for purchasing the diffractometer and Tulane University for support of the Tulane Crystallography Laboratory is gratefully acknowledged. Thanks go to the reviewers of this article for their comments.

Appendix A. Supplementary material

Supplementary data to this article can be found online at https://doi.org/10.1016/j.arabjc.2021.103595.

References

Abad, N., Sallam, H.H., Al-Ostoot, F.H., Khamees, H.A., Al-horaibi, S.A., A, S.M., Khanum, S.A., Madegowda, M., Hafi, M.E., Mague, J.T., Essassi, E.M., Ramli, Y., 2021. Ramli Synthesis, crystal structure, DFT calculations, Hirshfeld surface analysis, energy frameworks, molecular dynamics and docking studies of novel isoxazolequinoxaline derivative (IZQ) as anti-cancer drug. J. Mol. Struct. 1232, 130004. https://doi.org/10.1016/j.molstruc.2021.130004.

Abad, N., Ferfra, S., Essassi, E.M., Mague, J.T., Ramli, Y., 2021. Synthesis and crystal structure of 1-octyl-3-phenylquinoxalin-2 (1H)-one, $C_{22}H_{26}N_2O$. Zeitschrift für Kristallographie-New Cryst. Struct. 236, 173–175. https://doi.org/10.1515/ncrs-2020-0404.

Abad, N., Sallam, H.H., Al-Ostoot, F.H., Khamees, H.A., Al-horaibi, S.A., A, S.M., Khanum, S.A., Madegowda, M., Hafi, M.E., Mague, J.T., Essassi, E.M., Ramli, Y., 2021. Synthesis, crystal structure, DFT calculations, Hirshfeld surface analysis, energy frameworks, molecular dynamics and docking studies of novel isoxazolequinoxaline derivative (IZQ) as anti-cancer drug. J. Mol. Struct. 1232, 130004. https://doi.org/10.1016/j.molstruc.2021.130004.

Abdel-Rahman, L.H., Basha, M.T., Al-Farhan, B.S., Shehata, M.R., Mohamed, S.K., Ramli, Y., 2022. [Cu(dipicolinoylamide)(NO_3)(H_2O)] as anti-COVID-19 and antibacterial drug candidate: design, synthesis, crystal structure, DFT and molecular docking. J. Mol. Struct. 1247, 131348. https://doi.org/10.1016/j.molstruc.2021.131348.

Abramo, J.M., Reynolds, A., Crisp, G.T., Weurlander, M., Söderberg, M., Scheja, M., Hult, H., Wernerson, A., Emacs, A., 2012. UE Distribution, W. Makes, A. Like, O. Text, OT Editors, TA Interface, DC Sets, TR Look, E. Veterans, K. Bindings, C. Aquamacs, T.E.X. Support, TEX Previewer, C. Beaumont, M. O'Doherty, L. Shannon, D. Baume, MY, M. Coffey, A. Bhatara, P. Laukka, D.J. Levitin, A.-A. Darrow, W. Hornby, B. Gingras, I. Symposium, PS Isbn, T. Author, a EC All, A. Majid, L. Boroditsky, A. Gaby, M. Petre, G. Rugg, Individuality in music performance, Assess. Eval. High. Educ. 37, 435. https://doi.org/doi:10.1007/82.

Alsafi, M.A., Hughes, D.L., Said, M.A., 2020. First COVID-19 molecular docking with a chalcone-based compound: synthesis, single-crystal structure and Hirshfeld surface analysis study. Acta Crystallogr. Sect. C Struct. Chem. 76 (12), 1043–1050.

Asadi, Z., Esrafili, M.D., Vessally, E., Asnaashariisfahani, M., Yahyaei, S., Khani, A., 2017. A structural study of fentanyl by DFT calculations, NMR and IR spectroscopy. J. Mol. Struct. 1128, 552–562. https://doi.org/10.1016/j.molstruc.2016.09.027.

Bhatia, S., Giri, S., Lal, A.F., Singh, S., 2020. Identification of potential inhibitors of dietary polyphenols for SARS-CoV-2 M protease: an in silico study Identification of potential inhibitors of dietary polyphenols for SARS-CoV-2 M protease: An in silico study. Trop. Public Heal. 1, 21–29.

Brandau, S., Landa, A., Franze'n, J., Marigo, M., Jørgensen, K.A., 2006. Organocatalytic conjugate addition of malonates to a, bunsaturated aldehydes: asymmetric formal synthesis of (–)-paroxetine, chiral lactams, and lactones. Angew. Chem. 118, 4411–4415. https://doi.org/10.1002/anie.200601025.

Brandenburg, K., Putz, H., 2012. Diamond. Crystal Impact GbR, Bonn, Germany.

Bruker, 2016. APEX3, SAINT, SADABS & SHELXTL. Bruker AXS, Inc., Madison, WI.

Campochiaro, C., Della-Torre, E., Cavalli, G., De Luca, G., Ripa, M., Boffini, N., Tomelleri, A., Baldissera, E., Rovere-Querini, P., Ruggeri, A., Monti, G., De Cobelli, F., Zangrillo, A., Tresoldi, M., Castagna, A., Dagna, L., 2020. Efficacy and safety of tocilizumab in severe COVID-19 patients: a single-centre retrospective cohort study. Eur. J. Intern. Med. 76, 43–49. https://doi.org/10.1016/j.ejim.2020.05.021.

Cantini, F., Niccoli, L., Matarrese, D., Nicastri, E., Stobbione, P., Goletti, D., 2020. Baricitinib therapy in COVID-19: A pilot study on safety and clinical impact. J. Infect. 81 (2), 318–356. https://doi.org/10.1016/j.jinf.2020.04.017.

Cao, B., Wang, Y., Wen, D., Liu, W., Wang, J., Fan, G., Ruan, L., Song, B., Cai, Y., Wei, M., Li, X., Xia, J., Chen, N., Xiang, J., Yu, T., Bai, T., Xie, X., Zhang, L.i., Li, C., Yuan, Y.e., Chen, H., Li, H., Huang, H., Tu, S., Gong, F., Liu, Y., Wei, Y., Dong, C., Zhou, F., Gu, X., Xu, J., Liu, Z., Zhang, Y.i., Li, H., Shang, L., Wang, K. e., Li, K., Zhou, X., Dong, X., Qu, Z., Lu, S., Hu, X., Ruan, S., Luo, S., Wu, J., Peng, L.u., Cheng, F., Pan, L., Zou, J., Jia, C., Wang, J., Liu, X., Wang, S., Wu, X., Ge, Q., He, J., Zhan, H., Qiu, F., Guo, L.i., Huang, C., Jaki, T., Hayden, F.G., Horby, P.W., Zhang, D., Wang, C., 2020. A trial of lopinavir-ritonavir in adults hospitalized with severe Covid-19. N. Engl. J. Med. 382 (19), 1787–1799.

Cavalli, G., De Luca, G., Campochiaro, C., Della Torre, E., Roipa, M., 2020. Canetti D et al., Interleukin-1 blockade with high-dose anakinra in patients with COVID-19, acute respiratory distress syndrome, and hyperinflammation: a retrospective cohort stud. Lancet Rheumatol. 2, 325–331. https://doi.org/10.1016/S2665-9913(20)30127-2.

Colaneri, M., Bogliolo, L., Valsecchi, P., Sacchi, P., Zuccaro, V., Brandolino, F., et al, 2020. Microorganisms 8, 695. https://doi.org/10.3390/microorganisms8050695.

DeLano, W.L., 2004. PyMOL Reference Guide. Delano Sci, San Carlos, CA, US.

Dennington, R., Keith, T., Millam, J., 2009. GaussView, Version 5. Semichem Inc., Shawnee Mission, KS.

Dewangan, D., Nakhate, K.T., Verma, V.S., Nagori, K., Badwaik, H., Nair, N., Tripathi, D.K., Mishra, A., 2018. Synthesis and molecular docking study of novel hybrids of 1, 3, 4-oxadiazoles and quinoxaline as a potential analgesic and anti-inflammatory agents. J. Heterocycl. Chem. 55 (12), 2901–2910. https://doi.org/10.1002/jhet.v55.1210.1002/jhet.3363.

Druzhilovskiy, D.S., Rudik, A.V., Filimonov, D.A., Gloriozova, T.A., Lagunin, A.A., Dmitriev, A.V., Pogodin, P.V., Dubovskaya, V.I., Ivanov, S.M., Tarasova, O.A., Bezhentsev, V.M., Murtazalieva, K. A., Semin, M.I., Maiorov, I.S., Gaur, A.S., Sastry, G.N., Poroikov, V.V., 2017. Computational platform Way2Drug: from the prediction of biological activity to drug repurposing. Russ. Chem. Bull. 66, 1832–1841. https://doi.org/10.1007/s11172-017-1954-x.

El Aoufir, Y., Lgaz, H., Bourazmi, H., Kerroum, Y., Ramli, Y., Guenbour, A., Salghi, R., El-Hajjaji, F., Hammouti, B., Oudda, H. J., 2016. Mater. Environ. Sci. 7, 4330–4347. https://doi.org/10.13140/RG.2.2.23519.25766.

Frisch, M.J., Trucks, G.W., Schlegel, H.B., Scuseria, G.E., Robb, M. A., Cheeseman, J.R., Scalmani, G., Barone, V., Mennucci, B., Petersson, G.A., Nakatsuji, H., Caricato, M., Li, X., Hratchian, H. P., Izmaylov, A.F., Bloino, J., Zheng, G., Sonnenberg, J.L., Hada, M., Ehara, M., Toyota, K., Fukuda, R., Hasegawa, J., Ishida, M., Nakajima, T., Honda, Y., Kitao, O., Nakai, H., Vreven, T.,

Montgomery, J.A., Peralta, J.E., Ogliaro, F., Bearpark, M., Heyd, J.J., Brothers, E., Kudin, K.N., Staroverov, V.N., Keith, T., Kobayashi, R., Normand, J., Raghavachari, K., Rendell, A., Burant, J.C., Iyengar, S.S., Tomasi, J., Cossi, M., Rega, N., Millam, J.M., Klene, M., Knox, J.E., Cross, J.B., Bakken, V., Adamo, C., Jaramillo, J., Gomperts, R., Stratmann, R.E., Yazyev, O., Austin, A.J., Cammi, R., Pomelli, C., Ochterski, J.W., Martin, R.L., Morokuma, K., Zakrzewski, V.G., Voth, G.A., Salvador, P., Dannenberg, J.J., Dapprich, S., Daniels, A.D., Farkas, O., Foresman, J.B., Ortiz, J.V., Cioslowski, J., Fox, D.J., 2010. Gaussian 09, Revision C.01. Gaussian Inc, Wallingford CT.

Gilman, J.J., 2007. Bond modulus and stability of covalent solids. Philos. Mag. Lett. 87 (2), 121–124. https://doi.org/10.1080/09500830601166974.

Guerrab, W., Lgaz, H., Kansiz, S., Mague, J.T., Dege, N., Ansar, M., Marzouki, R., Taoufik, J., Ali, I.H., Chung, I.-M., Ramli, Y., 2020. Synthesis of a novel phenytoin derivative: crystal structure, Hirshfeld surface analysis and DFT calculations. J. Mol. Struct. 1205, 127630. https://doi.org/10.1016/j.molstruc.2019.127630.

Guerrab, W., El Jemli, M., Akachar, J., Demirtaş, G., Mague, J.T., Taoufik, J., Ibrahimi, A., Ansar, M., Alaoui, K., Ramli, Y., 2021. Design, synthesis, structural and molecular characterization, toxicity, psychotropic activity and molecular docking evaluation of a novel phenytoin derivative: 3-decyl-5, 5-diphenylimidazolidine-2,4-dione. J. Biomol. Struct. Dyn. https://doi.org/10.1080/07391102.2021.1922096 Article in Press.

Guerrab, W., Missioui, M., Zaoui, Y., Mague, J.T., Ramli, Y., 2021. Synthesis and crystal structure of 2-azido-N-phenylacetamide, $C_8H_8N_4O$. Zeitschrift für Kristallographie-New Cryst. Struct. 236, 133–134. https://doi.org/10.1515/ncrs-2020-0409.

Guerreiro, D.D., de Lima, L.F., de Sá, N.A.R., Mbemya, G.T., Ferreira, A.C.A., Alves, B.G., Sant'anna Maranhão, S., do Ó Pessoa, C., Pinheiro, A.C., Nogueira, T.C.M., de Souza, M.V.N., de Figueiredo, J.R., Rodrigues, A.P.R., 2020. Sant'anna Maranhão et, Response of preantral follicles exposed to quinoxaline: a new compound with anticancer potential. Res. Vet. Sci. 128, 261–268. https://doi.org/10.1016/j.rvsc.2019.12.010.

Hinsberg, O., 1887. Liebigs Ann. Chem. 237, 1228.

Jin, Z., Du, X., Xu, Y., Deng, Y., Liu, M., Zhao, Y., Zhang, B., Li, X., Zhang, L., Peng, C., Duan, Y., Yu, J., Wang, L., Yang, K., Liu, F., Jiang, R., Yang, X., You, T., Liu, X., Yang, X., Bai, F., Liu, H., Liu, X., Guddat, L.W., Xu, W., Xiao, G., Qin, C., Shi, Z., Jiang, H., Rao, Z., Yang, H., 2020. Structure of Mpro from COVID-19 virus and discovery of its inhibitors. Nature 582, 289–293. https://doi.org/10.1038/s41586-020-2223-y.

Jin, Z., Du, X., Xu, Y., Deng, Y., Liu, M., Zhao, Y., Zhang, B., Li, X., Zhang, L., Peng, C., Duan, Y., Yu, J., Wang, L., Yang, K., Liu, F., Jiang, R., Yang, X., You, T., Liu, X., Yang, X., Bai, F., Liu, H., Liu, X., Guddat, L.W., Xu, W., Xiao, G., Qin, C., Shi, Z., Jiang, H., Rao, Z., Yang, H., 2020. Structure of Mpro from SARS-CoV-2 and discovery of its inhibitors. Nature 582, 289–293. https://doi.org/10.1038/s41586-020-2223-y.

Kim, D.Y., Huh, S.C., Kim, S.M., 2001. Tetrahedron Lett. 42, 6299. https://doi.org/10.1016/S0040-4039(01)01237-0.

Krause, L., Herbst-Irmer, R., Sheldrick, G.M., Stalke, D., 2015. J. Appl. Cryst. 48, 3–10. https://doi.org/10.1107/S1600576714022985.

Kulkarni, N.V., Revankar, V.K., Kirasur, B.N., Hugar, M.H., 2012. Transition metal complexes of thiosemicarbazones with quinoxaline hub: an emphasis on antidiabetic property. Med. Chem. Res. 21 (5), 663–671. https://doi.org/10.1007/s00044-011-9576-6.

Kuo, C.J., Liu, H.G., Lo, Y.K., Seong, C.M., Lee, K.I., Jung, Y.S., Liang, P.H., 2009. Individual and common inhibitors of coronavirus and picornavirus main proteases. FEBS Lett. 583, 549–555. https://doi.org/10.1016/j.febslet.2008.12.059.

Laabaissi, T., Benhiba, F., Rouifi, Z., Allali, M., Missioui, M., Ourrak, K., Oudda, H., Ramli, Y., Warad, I., Zarrouk, A., 2019. Int. J. Corros. Scale Inhib. 8, 241–256. https://doi.org/10.1016/j.heliyon.2020.e03939.

Lagunin, A.A., Dubovskaja, V.I., Rudik, A.V., Pogodin, P.V., Druzhilovskiy, D.S., Gloriozova, T.A., Filimonov, D.A., Sastry, N.G., Poroikov, V.V., Rishi, A., 2018. CLC-Pred: A freely available web-service for in silico prediction of human cell line cytotoxicity for drug-like compounds. PLoS ONE 13 (1), e0191838. https://doi.org/10.1371/journal.pone.019183810.1371/journal.pone.0191838.g00110.1371/journal.pone.0191838.t00110.1371/journal.pone.0191838.t00210.1371/journal.pone.0191838.t00310.1371/journal.pone.0191838.s00110.1371/journal.pone.0191838.s00210.1371/journal.pone.0191838.s00310.1371/journal.pone.0191838.s00410.1371/journal.pone.0191838.s00510.1371/journal.pone.0191838.s006.

Lagunin, A., Stepanchikova, A., Filimonov, D., Poroikov, V., 2000. PASS: prediction of activity spectra for biologically active substances. Bioinformatics 16, 747–748. https://doi.org/10.1093/bioinformatics/16.8.747.

Luo, P., Liu, Y.i., Qiu, L., Liu, X., Liu, D., Li, J., 2020. Tocilizumab treatment in COVID-19: A single center experience. J. Med. Virol. 92 (7), 814–818. https://doi.org/10.1002/jmv.v92.710.1002/jmv.25801.

Macrae, C.F., Edgington, P.R., McCabe, P., Pidcock, E., Shields, G. P., Taylor, R., Towler, M., Van De Streek, J., 2006. Mercury: Visualization and analysis of crystal structures. J. Appl. Crystallogr. 39, 453–457. https://doi.org/10.1107/S002188980600731X.

Missioui, M., Mortada, S., Guerrab, W., Serdaroğlu, G., Kaya, S., Mague, J.T., Essassi, E.M., Faouzi, M.E.A., Ramli, Y., 2021. Novel antioxidant quinoxaline derivative: Synthesis, crystal structure, theoretical studies, antidiabetic activity and molecular docking study. J. Mol. Struct. 1239, 130484. https://doi.org/10.1016/j.molstruc.2021.130484.

Missioui, M., Said, M.A., Demirtaş, G., Mague, J.T., Ramli, Y., 2022. Docking of Disordered Independent Molecules of Novel Crystal Structure of (N-(4-methoxyphenyl)-2-(3-methyl-2-oxo-3,4-dihydroquinoxalin-1(2H)-yl)acetamide as anti-Covid-19 and anti-Alzheimer's disease. Crystal structure, HSA/DFT/XRD. J. Mol. Struct. 1247, 131420. https://doi.org/10.1016/j.molstruc.2021.131420.

Nataraj, A., Balachandran, V., Karthick, T., Karabacak, M., Atac, A., 2012. FT-Raman, FT-IR, UV spectra and DFT and ab initio calculations on monomeric and dimeric structures of 3,5-pyridinedicarboxylic acid. J. Mol. Struct. 1027, 1–14. https://doi.org/10.1016/j.molstruc.2012.05.048.

Özdemir Tarı, G., Ceylan, Ü., Uzun, S., Ağar, E., Büyükgüngör, O., 2018. Synthesis, spectroscopic (FT-IR, UV–Vis), experimental (X-Ray) and theoretical (HF/DFT) study of: (E)-2-Chloro-N-((4-nitrocyclopenta-1,3-dienyl)methylene)benzenamine. J. Mol. Struct. 1174, 18–24. https://doi.org/10.1016/j.molstruc.2018.04.005.

Parsey, M., 2020. An open letter from Merdad Parsey, Chief Medical Officer. Gilead Sci. https://stories.gilead.com/articles/open-letter-from-merdad-par sey, (Accessed 22 October 2020).

Pasin, L., Cavalli, G., Navalesi, P., Sella, N., Landoni, G., Yavorovskiy, G., Valery, V., Zangrillo, A., Dagna, L., Monti, G., 2021. Eur. J. Int. Med. 86, 34–40. https://doi.org/10.1016/j.ejim.2021.01.016.

Patel, H.M., Bhardwaj, V., Sharma, P., Noolvi, M.N., Lohan, S., Bansal, S., Sharma, A., 2019. Quinoxaline-PABA bipartite hybrid derivatization approach: design and search for antimicrobial agents. J. Mol. Struct. 1184, 562–568. https://doi.org/10.1016/j.molstruc.2019.02.074.

Patel, S.B., Patel, B.D., Pannecouque, C., Bhatt, H.G., 2016. Design, synthesis and anti-HIV activity of novel quinoxaline derivatives. Eur. J. Med. Chem. 117, 230–240. https://doi.org/10.1016/j.ejmech.2016.04.019.

Prasad, S., Ojha, D.P., 2017. Vibrational spectra, electronic properties and effect of alkyl chain length on chemical stability of nematogens – A comparision using DFT and HF methods. Mol. Cryst. Liq. Cryst. 658 (1), 69–80. https://doi.org/10.1080/15421406.2017.1415656.

Quartuccio, L., Sonaglia, A., McGonagle, D., Fabris, M., Peghin, M., Pecori, D., De Monte, A., Bove, T., Curcio, F., Bassi, F., De Vita, S., Tascini, C., 2020. Profiling COVID-19 pneumonia progressing into the cytokine storm syndrome: results from a single Italian Centre study on tocilizumab versus standard of care. J. Clin. Virol. 129, 104444. https://doi.org/10.1016/j.jcv.2020.104444.

Ragoussis, V., Panopoulou, M., Ragoussis, N., 2004. Concise preparation of the (3E,5Z)-alkadienyl system. New approach to the synthesis of principal insect sex pheromone constituents. J. Agric. Food Chem. 52 (16), 5047–5051. https://doi.org/10.1021/jf049406b.

Ramli, Y., Essassi, E.M., 2015. Adv. Chem. Res. 27, 109–160. https://doi.org/10.1107/S2414314618008829.

Ramli, Y., Moussaif, A., Karrouchi, K., Essassi, E.M., 2014. J. Chem. 563406, 1–21. https://doi.org/10.1155/2014/563406.

Russell, C.D., Millar, J.E., Baillie, J.K., 2020. Clinical evidence does not support corticosteroid treatment for 2019-nCoV lung injury. Lancet 395 (10223), 473–475. https://doi.org/10.1016/S0140-6736(20)30317-2.

Sanders, J.M., Monogue, M.L., Jodlowski, T.Z., et al, 2020. JAMA 323, 1824–1836. https://doi.org/10.1001/jama.2020.6019.

Saranya, A.V., Ravi, S., Venkatachalapathi, S., 2013. Res. J. Chem. Sci. 1, 82. https://doi.org/10.1007/s11164-013-1153-9.

Serafin, K., Mazur, P., Bak, A., Laine, E., Tchertanov, L., Mouscadet, J.-F., Polanski, J., 2011. Ethyl malonate amides: a diketo acid offspring fragment for HIV integrase inhibition. Bioorg. Med. Chem. 19 (16), 5000–5005. https://doi.org/10.1016/j.bmc.2011.06.054.

Shah, B., Modi, P., Sagar, S.R., 2020. In silico studies on therapeutic agents for COVID-19: Drug repurposing approach. Life Sci. 252, 117652–117664. https://doi.org/10.1016/j.lfs.2020.117652.

Sheldrick, G.M., 2015. Acta Cryst. A 71, 3–8. https://doi.org/10.1107/S2053229614024218.

Sheldrick, G.M., 2015. Acta Cryst. A 71, 3–8. https://doi.org/10.1107/S2053273314026370.

Shen, Q.-K., Gong, G.-H., Li, G., Jin, M., Cao, L.-H., Quan, Z.-S., 2020. Discovery and evaluation of novel synthetic 5-alkyl-4-oxo-4, 5-dihydro-[1, 2, 4] triazolo [4, 3-a] quinoxaline-1-carbox-amide derivatives as anti-inflammatory agents. J. Enzyme Inhib. Med. 35 (1), 85–95. https://doi.org/10.1080/14756366.2019.1680658.

Shinkai, H., Onogi, S., Tanaka, M., Shibata, T., Iwao, M., Wakitani, K., Uchida, I.J., 1998. Med. Chem. 41, 1927. https://doi.org/10.1021/jm970771m.

Sogut, O., Can, M.M., Guven, R., Kaplan, O., Ergenc, H., Umit, T.B., Demir, O., Kaya, M., Akdemir, T., Cakmak, S., 2021. Safety and efficacy of hydroxychloroquine in 152 outpatients with confirmed COVID-19: a pilot observational study. Am. J. Emerg. Med. 40, 41–46. https://doi.org/10.1016/j.ajem.2020.12.014.

Srinivasarao, S., Nandikolla, A., Suresh, A., Ewa, A.-K., Głogowska, A., Ghosh, B., Kumar, B.K., Murugesan, S., Pulya, S., Aggarwal, H., Sekhar, K.V.G.C., 2020. Discovery of 1, 2, 3-triazole based quinoxaline-1, 4-di-N-oxide derivatives as potential anti-tubercular agents. Bioorg. Chem. 100, 103955. https://doi.org/10.1016/j.bioorg.2020.103955.

Tanoli, S.T., Ramzan, M., Hassan, A., Sadiq, A., Jan, M.S., Khan, F. A., Ullah, F., Ahmad, H., Bibi, M., Mahmood, T., Rashid, U., Rodríguez Núñez, Y.A., Gutierrez, M., Alzate-Morales, J., Adasme-Carreño, F., Güiza, F.M., Bernal, C.C., Romero Bohórquez, A.R., Synthesis, P., Docking, M., Studies, D.F.T., Rivera, A., 2020. Design, synthesis and bioevaluation of tricyclic fused ring system as dual binding site acetylcholinesterase inhibitors. Int. J. Mol. Sci. 83, 1–25. https://doi.org/10.1016/j.bioorg.2018.10.035.

Tazouti, A., Galai, M., Touir, R., Touhami, M.E., Zarrouk, A., Ramli, Y., Saracoglu, M., Kaya, S., Kandemirli, F., Kaya, C., 2016. J. Mol. Liq. 221, 815–832. https://doi.org/10.1016/j.molliq.2016.03.083.

Thakuria, H., Das, G., 2006. One-pot efficient green synthesis of 1, 4-dihydro-quinoxaline-2, 3-dione derivatives. Int. J. Chem. Sc. 118 (5), 425–428. https://doi.org/10.1007/BF02711453.

Trott, O., Olson, A.J., 2009. AutoDock Vina: Improving the speed and accuracy of docking with a new scoring function, efficient optimization, and multithreading. J. Comput. Chem. 31, 455–461. https://doi.org/10.1002/jcc.21334.

Turner, M.A., Mckinnon, M.J., Wolff, J.J., Grimwood, S.K., Spackman, D.J., Jayatilaka, P.R., Spackman, D., 2017. CrystalExplorer. Version 17. The University of Western Australia, CrystalExplorer. Version 17. Univ. West. Aust.

Vraj Shah, D.S., Bhaliya, J., 2020. In silico study of 1,5-bis(4-hydroxy-3-methoxyphenyl)-1,4-pentadiene-3-one (deketene curcumin) on crystallized protein structures of SARS-CoV-2. ChemRxiv. 19, 1–15. https://doi.org/10.26434/chemrxiv.12377000.v1.

Wallace, A.C., Laskowski, R.A., Thornton, J.M., 1995. Ligplot: a program to generate schematic diagrams of protein-ligand interactions. Protein Eng. Des. Sel. 8, 127–134. https://doi.org/10.1093/protein/8.2.127.

Wheeler, T.N., 1984. Synthesis and insecticidal activities of pyrethroids derived from 3-methyl-2-(3,4-dihydronaphthyl) butanoic acids. J. Agric. Food Chem. 32 (5), 1125–1129. https://doi.org/10.1021/jf00125a049.

Woo, E.R., Fujii, I., Ebizuka, Y., Sankawa, U., Kawaguchi, A., Huang, S., Beale, J.M., Shibuya, M., Mocek, U., Floss, H.G., 1989. Nonstereospecific proton removal in the enzymatic formation of orsellinic acid from chiral malonate. J. Am. Chem. Soc. 111 (14), 5498–5500. https://doi.org/10.1021/ja00196a084.

Wu, S., Qi, L.e., Ren, Y., Ma, H., 2020. 1,2,4-triazole-3-thione Schiff bases compounds: crystal structure, hirshfeld surface analysis, DFT studies and biological evaluation. J. Mol. Struct. 1219, 128591. https://doi.org/10.1016/j.molstruc.2020.128591.

Xiao, H., Li, P., Hu, D.Y., Song, B.A., 2014. Bioorg. Med. Chem. Lett. 24, 3452. https://doi.org/10.1016/j.bmcl.2014.05.073.

Xing, Y.J., Lou, L.G., Chen, X.Z., Ye, Q.S., Xu, Y.P., Xie, C.Y., Jiang, J., Liu, W.P., 2012. Bioorg. Med. Chem. Lett. 22, 2239. https://doi.org/10.1016/j.bmcl.2012.01.091.

Zaoui, Y., Ramli, Y., Tan, S.L., Tiekink, E.R.T., Chemlal, L., Mague, J.T., Taoufik, J., Faouzi, M.E.A., Ansar, M.H., 2021. Synthesis, structural characterization and theoretical studies of a novel pyridazine derivative: Investigations of anti-inflammatory activity and inhibition of α-glucosidase. J. Mol. Struct. 1234,. https://doi.org/10.1016/j.molstruc.2021.130177 130177.

Zarrok, H., Zarrouk, A., Salghi, R., Oudda, H., Hammouti, B., Ebn Touhami, M., Bouachrine, M., Pucci, O., 2012. H. Electrochim. Acta 30, 405–417. https://doi.org/10.1016/j.molliq.2016.07.046.